Surface Magneto-Optic Kerr Effect of NiCo/Cu Multilayers

by

Xiaodong Meng

Department of Physics

McGill University

Montréal, Québec, Canada

November 1994

A Thesis Submitted to

the Faculty of Graduate Studies and Research

in Partial Fulfillment of the Requirements for the Degree of

Master of Science

ISBN 0-612-05599-X

Abstract

A phenomenological theory of magneto-optic Kerr effect (MOKE) is presented to illustrate the connection between the magnetization and the polarization of light reflection in an isotropic medium. An apparatus measuring the MOKE of magnetic medium was designed and constructed. The surface magneto-optic Kerr effect (SMOKE) of a magnetic multilayer is a measurement of the average magnetization of several layers within the penetration depth of the light.

SMOKE measurements on a series of sputtered $Ni_{80}Co_{20}15Å/Cu(t_{Cu})$, where t_{Cu} is the thickness of Cu spacer layer, multilayers confirms that the coupling strength in these multilayers oscillates from antiferromagnetic (AF) coupling to ferromagnetic coupling as a function of Cu spacer layer thickness. Low-angle x-ray diffraction and SMOKE measurements on a series of AF-coupled $(Ni_{80}Co_{20}15Å/Cu20Å)\times N$ multilayers with bilayer numbers N ranging from 8 to 100 shows that cumulative interface roughness increases with increasing N, as do the saturation field and coercivity. This is possibly due to the out-of-plane anisotropy associated with cumulative interface roughness in multilayers.

An AF-coupled $(Ni_{70}Co_{30}15Å/Cu20Å)\times$ 10 was continually annealed up to 400^0C in several steps, and the magnetic behaviour of the sample was evaluated as a function of annealing temperatures. $(Ni_{70}Co_{30}15Å/Cu20Å/Ni_{70}Co_{30}30Å/Cu20Å)\times5$ multilayer was used for investigating the AF coupling between magnetic layers of unequal thicknesses. Finally, an AF-coupled $(Ni_{70}Co_{30}15Å/Cu20Å/Ni_{70}Co_{30}15Å/Cu35Å)\times5$ multilayer was sputtered and used to study the magnetization of an AF-coupled multilayer with two different coupling strengthes.

Résumé

Afin d'illustrer la relation entre l'aimantation et la polarisation de lumiè réfléchie dans un médium isotropique, une théorie phénoménologique de l'effet de Kerr magnéto-optique (EKMO) a été dévelopée. Un appareil mesurant l'EKMO de millieu aimantés fût dessiné et construit. L'effet de Kerr magnéto-optique de surface (EKMOS) de multicouches magnétiques est une mesure de la magnétisation moyenne de plusieurs couches limité par la longueur de pénétration de la lumière.

Des mesures d'EKMOS sur une série d'échantillOns de $Ni_{80}Co_{20}15Å/Cu(t_{Cu})$, où t_{Cu} est l'épaisseur des couches d'espacement de cuivre, confirment que la force de couplage entre ces multicouches oscille, passant d'un couplage antiferromagnétique (AF) jusqu'à ferromagnétique, en fonction de l'épaisseur de la couche d'espacement de cuivre. Des mesures de diffraction aux rayons-x ainsi que les mesures d'EKMOS sur une série d'échantillons multicouches couplées AF $(Ni_{80}Co_{20}15Å/Cu20Å)\times N$ dont le nombre bicouche N varient de 8 à 100 démontrent que la rugosité de la surface cumulative augmente lorsque N augmente, tout comme le champ de saturation et la coercitivité. Ceci est possible grâce à l'anisotropie hors des plans associée avec la rugosité de surface cumulative des multicouches.

Le comportement magnétique d'un échantillon couplé AF $(Ni_{70}Co_{30}15Å/Cu20Å)\times 10$, recuit jusqu'à $400°C$ en plusieurs étapes, a été évalué en fonction de la temperature. Des échantillons multicouche de $(Ni_{70}Co_{30}15Å/Cu20Å/Ni_{70}Co_{30}30Å/Cu20Å)\times 5$ furent utilisés pour observer le couplage entre des couches magnétiques d'épaisseurs inégales. Finalement, un échantillon multicouche $(Ni_{70}Co_{30}15Å/Cu20Å/Ni_{70}Co_{30}15Å/Cu35Å)\times 5$ fût évaporé et utilisé afin d'étudier la aimentation de multicouches couplées AF ayant deux longueurs de couplage différentes.

Contents

List of Figures

List of Tables

Acknowledgement

I wish to take this opportunity to thank my supervisor, Prof W. Burnett Muir, for suggesting a project which was suited to my interest, managing my financial support, and advising on my research with resourcefulness and kindness.

I am greatly indebted to Prof Zaven Altounian for his constant advice on my work, Prof John O. Ström-Olsen for his interest in this project, Prof Mark Sutton for his enlightening comments on low-angle x-ray reflectivity measurement involved, and Prof Robert W. Cochrane for giving me access to his laboratory for magnetoresistance measurement in Départment de Physique, Université de Montréal.

I would like to thank my fellow graduate students. Xiaoping Bian generously offered his help and comments on many important issues throughout this project; Yi Zhao let me share his knowledge on computer-controlled data aquisition; Randa Abdouche helped me fit low-angle x-ray reflectivity data; and Stéphane Legault translated the abstract into French. I enjoyed the warm and active atmosphere on the 4th floor of Rutherford Physics Building with, just name a few, Quanmin Yang, Tianqu Gu, Ke Xin, Erol Girt, Mosen Sabouri, Eric Dufresne, Yanbin Wang, Ou Mao, Zhida Yan, Yongjiang Wang, *et al.*. Happy memory also goes back to my early days of graduate study at McGill when I received friendly assistance from Weimin Wang, Ricardo Anino, and Pierre Laperle.

I am grateful to Frank Van Gils and John Egyed for their technical help, Cynthia MacDonald, Paula Domingues, Joanne Longo, and Diane Koziol for their administrative assistance.

My last thank goes to my wife, Qin Xin, for her patience throughout my graduate study.

Xiaodong Meng

Rutherford Physics Building
McGill University

Chapter 1

Introduction

1.1 Magneto-Optic Effects: MOKE and MOFE

Our understanding of magneto-optic effects is historically rooted in the work of M. Faraday[1] and J. Kerr[2]. They were the first to study the influence of magnetized media on the polarization of transmitted and reflected light respectively. When linearly polarized light is transmitted through a magnetized medium, the polarization of the transmitted light rotates by an angle α, as shown in Fig. 1.1. This is named *the magneto-optic Faraday effect* (MOFE); when linearly polarized light is reflected from the surface of a magnetized medium, the reflected light becomes elliptically polarized with a rotation of the polarization plane, as shown in Fig. 1.2. This is named *the magneto-optic Kerr effect* (MOKE). These two magneto-optic effects are due to the interaction between light and the magnetized medium, and give the information on the electronic and magnetic structure of the medium. Since their discovery, they have been widely used in diverse areas of research and technology.

Due to the connection between the magnetization of the medium and the rotation of the polarization plane of the reflected light, the MOKE is a widely used magnetic measurement technique in the search for new magneto-optic information storage media. Several modulation methods have been developed to precisely measure the rotation and ellipticity of the polarization of the reflected light, such as the Fara-

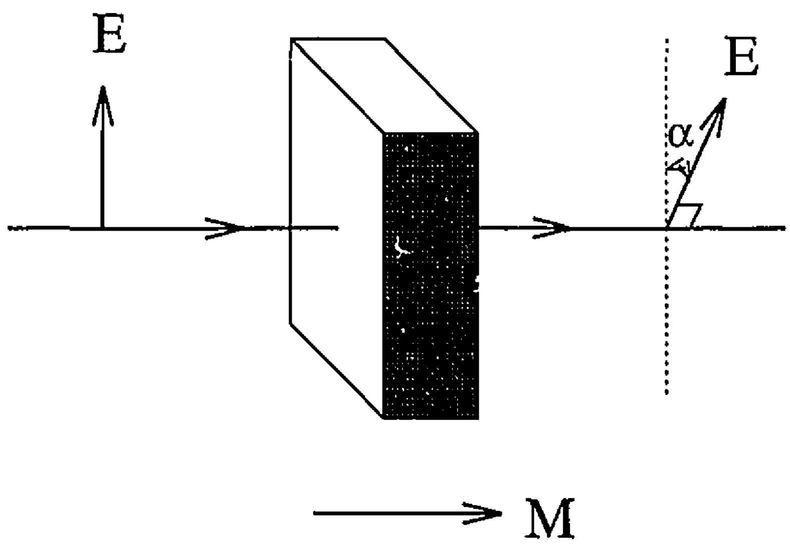

Figure 1.1: MOFE: rotation of the polarization plane of linearly polarized light after transmiting through a magnetized medium

day cell technique [3], the spinning analyzer technique [4], and the piezo-birefringent modulator [5]. A novel magneto-optic microscope system using a digital contrast enhancement scheme has also been devised to observe magnetic domain dynamics [6].

It is customary to distinguish three principal cases of MOKE according to the geometry of the experiment. They are:

1) Polar MOKE (see Fig. 1.3(a)): the magnetization direction is perpendicular to the surface of the medium and parallel to the plane of incidence;

2) Longitudinal MOKE (see Fig. 1.3(b)): the magnetization is parallel to the surface of the medium and parallel to the plane of light incidence;

3) Transverse MOKE (see Fig. 1.3(c)): the magnetization lies in the surface of

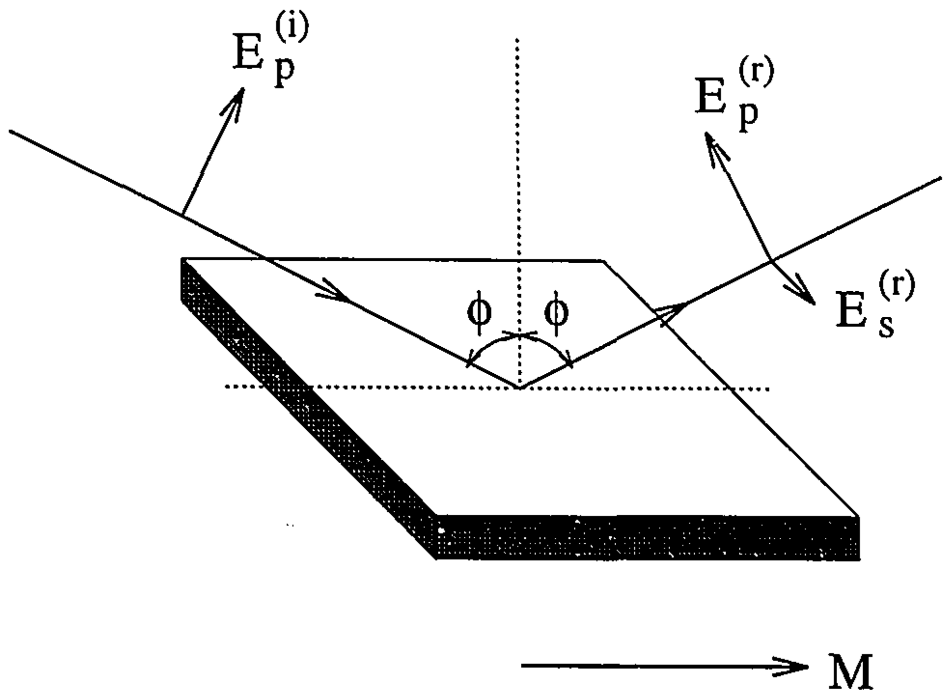

Figure 1.2: MOKE: change in the polarization state of linearly polarized light upon reflection by a magnetized medium's mirror surface. Note that E_p^r and E_s^r are generally not in phase.

the medium and is normal to the plane of incidence.

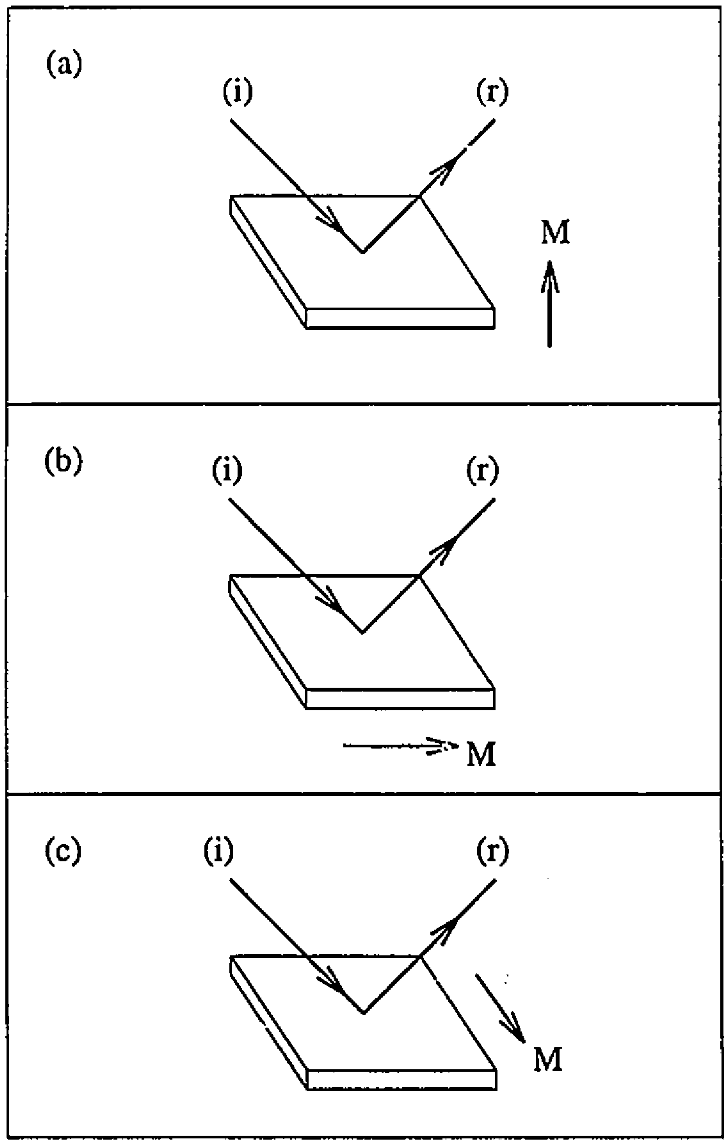

Figure 1.3: Illustrations of three categories of MOKE: (a) Polar MOKE; (b) Longitudinal MOKE; (c) Transverse MOKE.

1.2 Magnetic Multilayers and SMOKE

1.2.1 Magnetic Multilayers

Artificially made and ordered material systems are an important part of late-20th-century advanced technology. Among them, magnetic multilayers, or magnetic superlattices, have exhibited new and interesting physical effects which show great potential for technological advances in information storage and retrieval, including magnetic read heads and magnetic field sensors for a variety of applications.

Magnetic multilayers are made by the orderly deposition of alternating thin films of two or more metals, at least one of which is magnetic. These materials display many interesting phenomena, such as, superconductivity[7], solid-state amorphization[8], interdiffusion[9], low-dimensional magnetism[10], and more recently, magnetic interlayer exchange coupling[11–13], and giant magnetoresistance[12,13].

Interest in magnetic multilayers has been encouraged by the availability of improved sample preparation techniques, such as sputtering, molecular beam epitaxy (MBE), and chemical deposition [14,15], and by the rapid development of sophisticated characterization techniques[15], such as, low energy electron diffraction (LEED), reflective high-energy electron diffraction (RHEED), Auger electron spectroscopy (AES), transmission electron microscopy (TEM), low-angle x-ray diffraction (LXD), and surface magneto-optic Kerr effect (SMOKE).

Metallic multilayers constructed of thin magnetic layers separated by thin non-magnetic layers have been used to study magnetic coupling mediated by non-magnetic metals[16]. In experiments from the 1960's until about 1988, however, the coupling of such magnetic layers through most metals was found to be ferromagnetic[17]. Only recently an oscillating magnetic coupling of the well-known Ruderman-Kittel-Kasuya-Yosida (RKKY) form[18]) was observed in the majority of transition metal multilayers[12,19,20].

The first evidence for antiferromagnetic (AF) coupling of magnetic layers via a transition metal was made in crystalline bcc (100) Fe/Cr/Fe sandwiches[11] using

Brillouin light scattering and SMOKE hysteresis loops. Interest in the AF coupling was heightened by the subsequent observation that the resistance of the AF-coupled (100) Fe/Cr/Fe sandwiches [21], (100) Fe/Cr multilayers[13] and the sputtered Fe/Cr multilayers[12] decrease enormously with the application of a magnetic field. The changes are so large that the phenomenon has been termed *giant magnetoresistance* (GMR). Later on, the AF coupling and associated GMR were found in multilayers from other combination of transition and noble metals, especially in Cu-based multilayers such as Co/Cu[19], NiFe/Cu, NiFeCo/Cu[22,23], and NiCo/Cu[24,25]. Studies on these multilayers with increasing spacer thickness evidently show oscillations in the strenght of the AF interlayer coupling and in the magnetoresistance (MR) variations.

1.2.2 MOKE and SMOKE

Magnetic hysteresis measurement is an important step in the characterization magnetic multilayers. MOKE provides an easy way to make these measurements. We emphasize that the MOKE of magnetic multilayers is not the same as that in bulk magnetic materials. In a multilayer light transmits through and is reflected from and absorbed in several ultrathin magnetic and non-magnetic layers, as shown in Fig. 1.4. The light which transmits through a magnetic layer before being reflected undergoes Faraday rotation on transmission as well as Kerr rotation upon reflection. The surface superlattice structure is also relevant. In order to distinguish this effect from the MOKE of bulk magnetic materials, it is called *the surface magneto-optic Kerr effect* (SMOKE).

Other magnetization measurement techniques, such as superconducting quantum interference device (SQUID) magnetometer, and vibrating sample magnetometer (VSM), measure the overall magnetization of the sample. The SMOKE magnetometer only measures the top few layers within the penetration depth of the light and reveals information about surface magnetism. These methods give complimentary results.

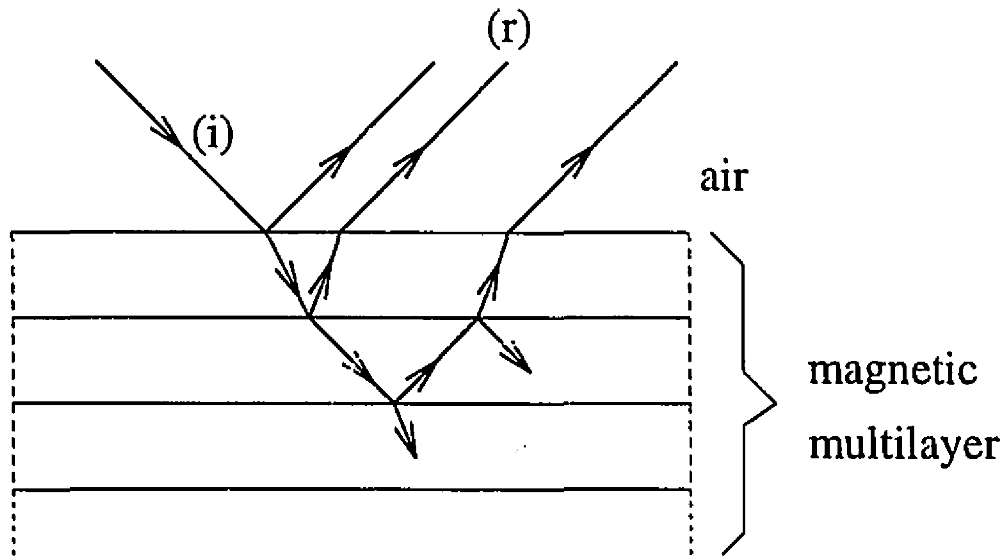

Figure 1.4: Magneto-optic scattering from a multilayer

Chapter 2

Theory of Magneto-Optic Effects

2.1 Introduction

Magnetism is an electrically driven phenomenon and quantum mechanical in nature. It has its origins in the Pauli exclusion principle and the existence of electron spin. A rigorous thorough treatment of magneto-optics should relate the optic transmission and reflection in magnetic media to atomic magnetic moments and crystal fields. Argyres[26] attempted this in 1955, taking into account spin-orbit interactions. However, quantum magneto-optics can only deal with the simplest cases using limiting approximations. Therefore the classical treatment is still widely used in data analysis.

The classical version of magneto-optics is phenomenological and is outlined in Landau and Lifshitz's *Electrodynamics of Continuous Media*[27]. Unfortunately, there is no comprehensive review of the magneto-optics of magnetic multilayers in the literature. Based on Ref.[27] and [28], we present a concise review of the subject starting from the fundamentals, with some reorganization and simplification.

In this chapter, we will discuss the dielectric properties of an isotropic bulk medium in the presence of a magnetic field, and derive the optical modes in such a medium. Magneto-optic Faraday and Kerr effect expressions then will come out naturally. The goal of this chapter is to obtain magneto-optic Kerr effect expressions which will facilitate the design of the Kerr effect measurement apparatus in Chapter 3.

2.2 Description of Polarized Light

Light is electromagnetic radiation with its frequency falling in the optical range with its wavelength from 4000 Å to 7600 Å. It is described by Maxwell's equations in the classical limit. For the physical effect of the field vectors on almost all media with which we are concerned, the electric field $\mathbf{E}$, instead of magnetic field $\mathbf{H}$, is the dominant constituent of light[28]. In Gaussian units, the mechanical force $\mathbf{F}$ of the field on a charged particle is given by Lorentz' law,

$$\mathbf{F} = q(\mathbf{E} + \frac{\mathbf{v}}{c} \times \mu\mathbf{H}), \tag{2.1}$$

q being the charge, μ the permeability, $\mathbf{v}$ the velocity of the particle, and c the velocity of light. Since v/c is usually very small compared to unity, the magnetic effect of light may often be neglected.

The simplest optical radiation is that of a monochromatic plane wave, i.e., when each component of $\mathbf{E}$ is of the form

$$E_{i_o} cos\,(\omega t - \mathbf{k} \cdot \mathbf{r} + \delta_i), \tag{2.2}$$

where E_{i_o} represents the amplitude of the ith scalar component of $\mathbf{E}$, ω the frequency, $\mathbf{k}$ the wave vector with $|\mathbf{k}| = \omega/c$, and δ_i the relative phase of the ith component; t and $\mathbf{r}$ are the time and space coordinates, respectively.

We choose to work in Cartesian coordinates $\{\ x,\ y,\ z\ \}$ with the z-axis in the $\mathbf{k}$ direction. The curve which the end point of the $\mathbf{E}$ vector describes is the locus of the points whose coordinates are:

$$\begin{aligned} E_x &= a_1 cos\,(\omega t - kz + \delta_1), \\ E_y &= a_2 cos\,(\omega t - kz + \delta_2), \\ E_z &= 0 \end{aligned} \tag{2.3}$$

and the first two equations can be rewritten into the form

$$\begin{aligned} \frac{E_x}{a_1} &= cos\,(\omega t - kz)\ cos\,(\delta_1) - sin\,(\omega t - kz)\ sin\ \delta_1, \\ \frac{E_y}{a_2} &= cos\,(\omega t - kz)\ cos\,(\delta_2) - sin\,(\omega t - kz)\ sin\ \delta_2. \end{aligned} \tag{2.4}$$

Squaring and adding gives

$$(\frac{E_x}{a_1})^2 + (\frac{E_y}{a_2})^2 - 2\frac{E_x}{a_1}\frac{E_y}{a_2}cos\ \delta = sin^2\delta, \tag{2.5}$$

where

$$\delta = \delta_1 - \delta_2, \tag{2.6}$$

which is the equation of an ellipse. The wave is then said to be *elliptically polarized.* The ellipse is inscribed into a rectangle whose sides are parallel to the coordinate axies and whose lengths are $2a_1$ and $2a_2$ (see Fig. 2.1). The ellipse touches the sides at the points $(\pm a_1, \pm a_2 cos\ \delta)$ and $(\pm a_1 cos\ \delta, \pm a_2)$.

The shape of the ellipse and its orientation can be fully described by specifying the ellipticity, i. e., the ratio of the minor to the major principal axes of the ellipse, and the azimuth θ , i.e., the angle between the major axis and the reference direction of x-axis. Alternatively, it will be convenient to introduce an auxiliary angle α $(0 \leq \alpha \leq \pi/2)$, such that

$$tan\ \alpha = \frac{a_2}{a_1}. \tag{2.7}$$

As shown in Ref. [29], the following expression for ellipticity θ and the azimuth ε can be obtained

$$\begin{aligned} sin\ 2\varepsilon = &\ sin\ 2\alpha\ sin\ \delta, \\ tan\ 2\theta = &\ tan\ 2\alpha\ cos\ \delta \end{aligned} \tag{2.8}$$

which are called *equation of polarimetry.* The polarization state of the light wave concerned can be fully described by either of the two equivalent sets of paramenters, θ and ε, or α and δ. Of these, the former set can be measured directly, while the latter is more convenient for mathematical operations.

If, instead of the real representation written above, the complex one is used, then

$$\begin{aligned} E_x = &\ a_1 e^{i(\omega t - kz + \delta_1)} \\ E_y = &\ a_2 e^{i(\omega t - kz + \delta_2)} \\ E_z = &\ 0. \end{aligned} \tag{2.9}$$

Thus, we have

$$\frac{E_y}{E_x} = \frac{a_2}{a_1}e^{i\delta}. \tag{2.10}$$

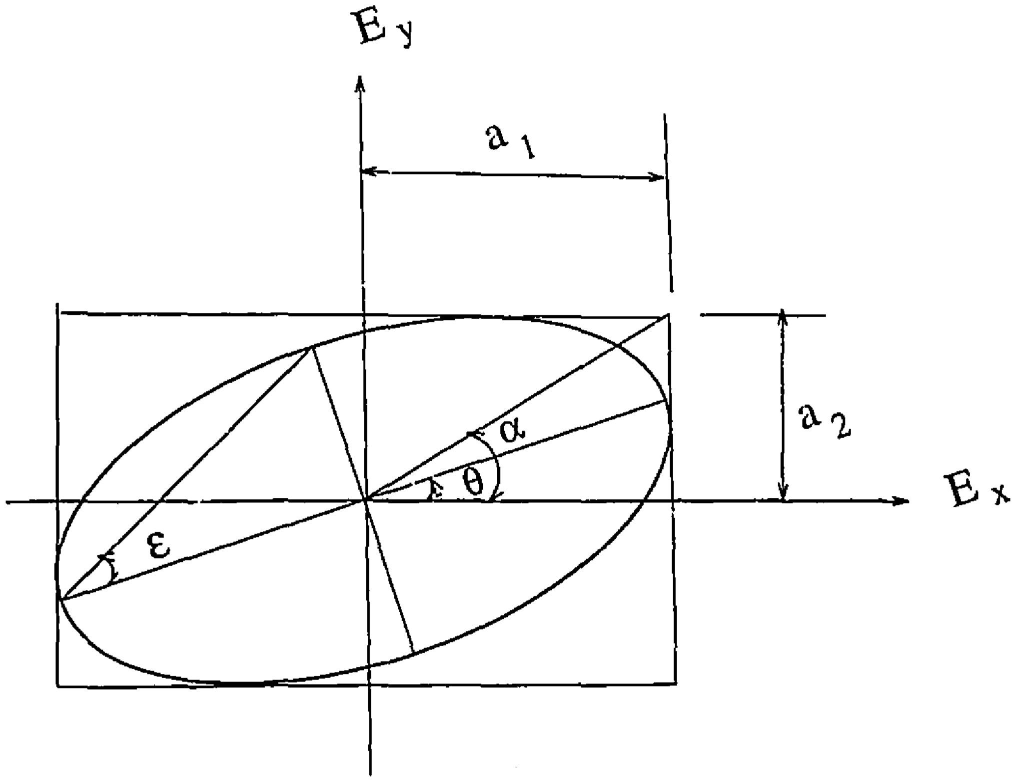

Figure 2.1: Quantities that describe elliptic polarization.

Here two special polarization states of particular importance can be determined from the value of δ. One is the linear polarization, namely when

$$\delta = \delta_2 - \delta_1 = m\pi \quad (m = 0, \pm 1, \pm 2, ...), \tag{2.11}$$

then

$$\frac{E_y}{E_x} = (-1)^m \frac{a_2}{a_1} \tag{2.12}$$

The other is the circular polarization, namely when

$$\begin{aligned} \delta = &\ m\pi/2 \quad (m = \pm 1, \pm 2, ...), \quad and \\ a_1 = &\ a_2, \end{aligned} \tag{2.13}$$

then

$$\frac{E_y}{E_x} = \pm i. \tag{2.14}$$

Here '+' represents the right-handed circular polarization and '−' the left-handed one. The **E** vector of a monochromatic electromagnetic plane wave can be written in the form of a 2×1 column vector as follows

$$\begin{aligned} E(z,t) &= \begin{bmatrix} E_x \\ E_y \end{bmatrix} \\ &= \begin{bmatrix} a_1 e^{i(\omega t - kz + \delta_1)} \\ a_2 e^{i(\omega t - kz + \delta_2)} \end{bmatrix} \\ &= e^{i(\omega t - kz)} \begin{bmatrix} a_1 e^{i\delta_1} \\ a_2 e^{i\delta_2} \end{bmatrix}. \end{aligned} \tag{2.15}$$

Because the **E** vector componets at all points in space for a monochromatic plane wave are known to oscillate harmonically with time at the same frequency, the temporal information can be suppressed. We can write

$$\mathbf{E} = \begin{bmatrix} E_x \\ E_y \end{bmatrix}. \tag{2.16}$$

with

$$\begin{aligned} E_x &= a_1 e^{i\delta_1}, \\ E_y &= a_2 e^{i\delta_2}. \end{aligned} \tag{2.17}$$

This **E** vector contains complete information about the polarization of the monochromatic plane wave light.

2.3 Magneto-Optic Effects of Magnetic Medium

2.3.1 Dielectric Properties of Magnetic medium

The behaviour of a medium under the influence of an electric field can be described by an dielectric constant ϵ which defines the relation between the electric field $\mathbf{E}$ and the displacement $\mathbf{D}$

$$\mathbf{D} = \epsilon \mathbf{E} \tag{2.18}$$

In an anisotropic medium, ϵ is a tensor of two-dimension. But in the great majority of cases, a medium can be supposed isotropic, and ϵ reduces to a complex scalar; thus, the relation between $\mathbf{D}$ and $\mathbf{E}$ is linear. Further, if the medium is non-absorbing, ϵ is a real scalar.

In discussing the mgneto-optic phenomena, we begin with a simple case where the medium is isotropic and non-absorbing in the absence of an applied magnetic field. In the form of a tensor expression we have

$$D_i = \epsilon_{ij} E_j \tag{2.19}$$

where

$$\epsilon_{ij} = \begin{bmatrix} \epsilon & 0 & 0 \\ 0 & \epsilon & 0 \\ 0 & 0 & \epsilon \end{bmatrix}, \tag{2.20}$$

and ϵ is a real scalar.

An effective dielectric tensor $\epsilon_{ij}(\mathrm{M})$ as a function of magnetization of the medium, M, will be used to describe the properties of a magnetically anisotropic medium which is isotropic in the absence of any magnetic field. $\epsilon_{ij}(\mathrm{M})$ satisfies the following Onsager relation[30],

$$\epsilon_{ij}(-\mathrm{M}) = \epsilon_{ij}(\mathrm{M}) \tag{2.21}$$

and the relation between vectors $\mathbf{D}$ and $\mathbf{E}$ becomes

$$D_i = \epsilon_{ij}(\mathrm{M}) E_j. \tag{2.22}$$

The energy loss, w, of light with frequency ω travelling in a medium with dielectric constant tensor ϵ is [31]

$$w = \frac{i\omega}{8\pi}(\epsilon_{ij}^{*} - \epsilon_{ji})E_i E_j^{*}, \tag{2.23}$$

and the condition that absorption in the medium is absent requires that the tensor ϵ should be Hermitian:

$$\epsilon_{ij} = \epsilon_{ji}^{*} \tag{2.24}$$

which implies that the real and imaginary parts of ϵ_{ij} must be respectively symmetric and antisymmetric, i. e., if

$$\epsilon_{ij} = \epsilon_{ij}^{'} + i\epsilon_{ij}^{''}, \tag{2.25}$$

then

$$\begin{aligned} \epsilon_{ij}^{'} &= \epsilon_{ji}^{'}, \\ \epsilon_{ij}^{''} &= -\epsilon_{ji}^{''}. \end{aligned} \tag{2.26}$$

Using (2.24), we have

$$\begin{aligned} \epsilon_{ij}^{'}(\mathrm{M}) &= \epsilon_{ji}^{'}(\mathrm{M}) = \epsilon_{ij}^{'}(-\mathrm{M}), \\ \epsilon_{ij}^{''}(\mathrm{M}) &= -\epsilon_{ji}^{''}(\mathrm{M}) = -\epsilon_{ij}^{''}(-\mathrm{M}). \end{aligned} \tag{2.27}$$

By expanding ϵ_{ij} to the linear term in M we conclude that tensor $\epsilon_{ij}^{'}$ reduces to a scalar notated as ϵ which is independent of M, and that $\epsilon_{ij}^{''}$ becomes an antisymmetric tensor which is proportional to M. Therefore (2.25) becomes

$$\epsilon_{ij} = \epsilon I + i\epsilon_{ij}^{''}, \quad \epsilon_{ij}^{''} = \begin{bmatrix} 0 & \epsilon_{12} & \epsilon_{13} \\ -\epsilon_{12} & 0 & \epsilon_{23} \\ -\epsilon_{13} & -\epsilon_{23} & 0 \end{bmatrix} \tag{2.28}$$

where I is a unit matrix.

Mathematically, the antisymmetric tensor $\epsilon_{ij}^{''}$ is equivalent to an axial vector **g**. For an isotropic medium, **g** is parallel to M and proportional to M in the linear approximation,

$$\mathbf{g} = f\mathbf{M} \tag{2.29}$$

where f is a proportionality coefficient. By using the notion of an antisymmetric unit tensor e_{ijk} we have

$$\epsilon''_{ij} = \sum_k e_{ijk} g_k. \tag{2.30}$$

The connection between the components of the dielectric tensor ϵ''_{ij} and the axial vector g is

$$\begin{aligned} g_1 &= \epsilon_{12}, \\ g_2 &= -\epsilon_{13}, \\ g_3 &= \epsilon_{23}. \end{aligned} \tag{2.31}$$

Therefore, (2.28) becomes

$$\epsilon_{ij} = \begin{bmatrix} \epsilon & ig_3 & -ig_2 \\ -ig_3 & \epsilon & ig_1 \\ ig_2 & -ig_1 & \epsilon \end{bmatrix}. \tag{2.32}$$

and (2.22) can be expressed in terms of vector g,

$$D_i = \epsilon E_i + i \sum_{j,k} e_{ijk} g_k E_j, \tag{2.33}$$

or, equivalently, in the form of vector expression,

$$\mathbf{D} = \epsilon \mathbf{E} + i \mathbf{E} \times \mathbf{g} \tag{2.34}$$

which can be inverted to give

$$\mathbf{E} = \frac{1}{\epsilon}\mathbf{D} - i\frac{1}{\mathbf{D}} \times \mathbf{g}. \tag{2.35}$$

Through equations (2.29), (2.32) and (2.33) we have established the relation between the dielectric tensor ϵ of a medium and its magnetization M. Up to now we have demonstrated how an isotropic medium previously possessing a real scalar dielectric constant has been changed into anisotropic medium under the influence of magnetization in the sense that the dielectric constant has become a tensor of rank two. Since optical propagation modes in an anisotropic medium are totally different from those in an isotropic one, it is expected that the optical reflectivity and refractivity will be dramatically changed once the medium is magnetized.

2.3.2 Optic Modes in Magnetic Medium

In a medium possessing no external current and assuming a unit permeability, $\mathbf{H} = \mathbf{B}$, and Maxwell's equation reads

$$\begin{aligned} \nabla \times \mathbf{H} &= \frac{1}{c}\frac{\partial \mathbf{D}}{\partial t}, \\ \nabla \times \mathbf{E} &= -\frac{1}{c}\frac{\partial \mathbf{H}}{\partial t}. \end{aligned} \tag{2.36}$$

Futhermore, for monochromatic plane wave light of a single frequency ω, both $\mathbf{H}$ and $\mathbf{E}$ are propotional to $e^{i(\mathbf{k}\cdot\mathbf{r}-\omega t)}$, and Maxwell's equation (2.36) become

$$\begin{aligned} \frac{\omega \mathbf{H}}{c} &= \mathbf{k} \times \mathbf{E}, \\ \frac{\omega \mathbf{D}}{c} &= -\mathbf{k} \times \mathbf{H}, \end{aligned} \tag{2.37}$$

and the three vectors $\mathbf{k}$, $\mathbf{D}$ and $\mathbf{H}$ are mutually perpendicular. We can define a refraction-index vector $\mathbf{n}$ by

$$\mathbf{k} = \frac{\omega \mathbf{n}}{c}. \tag{2.38}$$

From (2.37) and (2.38) we get

$$\begin{aligned} \mathbf{H} &= \mathbf{n} \times \mathbf{E}, \\ \mathbf{D} &= -\mathbf{n} \times \mathbf{H} \end{aligned} \tag{2.39}$$

which results in

$$\mathbf{D} = n^2\mathbf{E} - (\mathbf{E} \cdot \mathbf{n})\mathbf{n}. \tag{2.40}$$

We set up a coordinate system $\{ x, y, z\}$ inside the medium with z axis parellel to $\mathbf{n}$ (see Fig. 2.2). Thus,

$$n_x = n_y = 0, \quad and \quad n_z = n \neq 0, \tag{2.41}$$

and (2.40) decomposes into

$$\begin{aligned} D_x &= n^2 E_x, \\ D_y &= n^2 E_y, \\ D_z &= 0, \end{aligned} \tag{2.42}$$

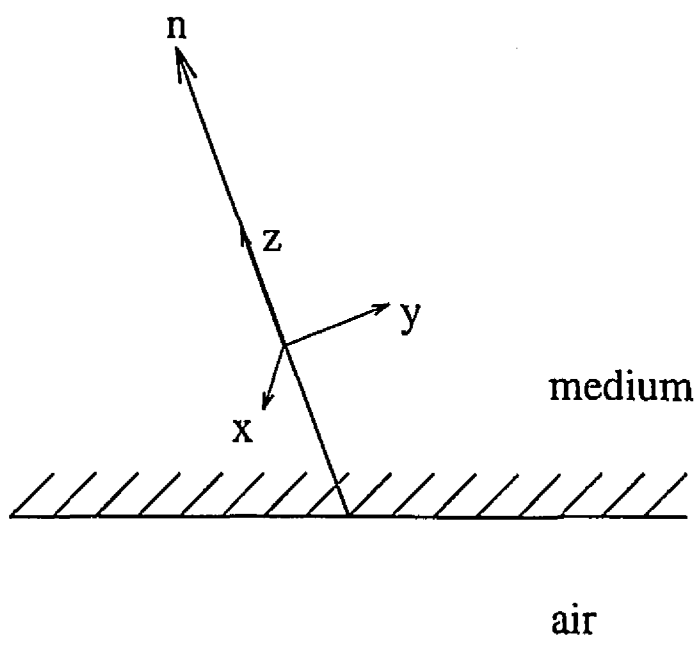

Figure 2.2: Direction of the wave normal, n.

or, inversely,

$$\begin{aligned} E_x &= \tfrac{1}{n^2} D_x, \\ E_y &= \tfrac{1}{n^2} D_y, \end{aligned} \tag{2.43}$$

and E_z is to be determined later.

Through (2.35) and (2.43) we establish relations for D_x and D_y,

$$\begin{aligned} (\tfrac{1}{n^2} - \tfrac{1}{\epsilon}) D_x + i\tfrac{g_3}{\epsilon} D_y &= 0, \\ -i\tfrac{g_3}{\epsilon} D_x + (\tfrac{1}{\epsilon} - \tfrac{1}{n^2}) D_y &= 0 \end{aligned} \tag{2.44}$$

where g_3 is the axial vector g's z-component. A non-vanishing **D** requires that the determinant of the coefficients should vanish,

$$\begin{vmatrix} \tfrac{1}{n^2} - \tfrac{1}{\epsilon} & i\tfrac{g_3}{\epsilon} \\ -i\tfrac{g_3}{\epsilon} & \tfrac{1}{n^2} - \tfrac{1}{\epsilon} \end{vmatrix} = 0 \tag{2.45}$$

which gives two solutions to the index of refrection, n_+ and n_-, respectively satisfying

$$\frac{1}{n_+^2} = \frac{1}{\epsilon} - \frac{g_3}{\epsilon} \tag{2.46}$$

and

$$\frac{1}{n_-^2} = \frac{1}{\epsilon} + \frac{g_3}{\epsilon}. \tag{2.47}$$

Corresponding to the two solutions, there are two modes of $\mathbf{D}$ satisfying

$$\frac{D_x}{D_y} = i \quad for \quad n_+ \tag{2.48}$$

and

$$\frac{D_x}{D_y} = -i \quad for \quad n_-. \tag{2.49}$$

Substituting (2.42) into (2.48) and (2.49) results in two modes for $\mathbf{E}$,

$$\frac{E_x}{E_y} = i \quad for \quad n_+, \tag{2.50}$$

and

$$\frac{E_x}{E_y} = -i \quad for \quad n_-, \tag{2.51}$$

with

$$E_z = 0. \tag{2.52}$$

It is concluded that light modes in a magnetized medium are two independent right-handed and left-handed circular polarizations, each with different indices of refraction n_+ and n_-, and hence with different wave vectors

$$k_\pm = \omega n_\pm / c. \tag{2.53}$$

It is easy to see that, if the medium is not magnetized, i. e., g_3=0, and n_+=n_-, the light mode is linearly polarized as expected.

2.3.3 Faraday Effect

Let a linearly polarized plane wave be incident normally on a medium and pass through a path l. Inside the medium the linear oscillation can be represented as the sum of two circular oscillations with opposite directions of rotation, which are then propagated through the medium with different wave vectors as expressed in (2.53). Arbitrarily taking the wave amplitude as unity, we have

$$\begin{aligned} E_x = & \tfrac{1}{2}(e^{ik_+z} + e^{ik_-z}), \\ E_y = & \tfrac{1}{2}i(-e^{ik_+z} + e^{ik_-z}), \end{aligned} \tag{2.54}$$

or, putting $k=\frac{1}{2}(k_+ + k_-)$ and $\kappa=\frac{1}{2}(k_+ - k_-)$,

$$\begin{aligned} E_x = & e^{ikz} cos\ \kappa z, \\ E_y = & e^{ikz} sin\ \kappa z. \end{aligned} \tag{2.55}$$

When the wave leaves the slab, we have

$$\frac{E_y}{E_x} = tan\ \kappa l. \tag{2.56}$$

Since this ratio is real, the two beams merge into a linearly polarized beam but with a non-zero polarization rotation away from its incident one. This is *the Faraday effect.*

2.3.4 Kerr Effect

When a linear polarized beam is reflected from the mirror surface of a magnetized medium, the reflected beam is then rendered elliptically polarized together with a rotation of its polarization plane. This is *the Kerr effect.* We will present a detailed consideration of this case.

In magneto-optics, the dielectric tensor ϵ_{ij} is usually expressed in terms of *the magneto-optic coupling vector*, or *the Voigt vector* [32], $\mathbf{Q}$,

$$\mathbf{Q} = \mathrm{g}/\epsilon = f\mathrm{M}/\epsilon, \tag{2.57}$$

and (2.32) becomes

$$\epsilon_{ij} = \epsilon \begin{bmatrix} 1 & iQ_3 & -iQ_2 \\ -iQ_3 & 1 & iQ_1 \\ iQ_2 & -iQ_1 & 1 \end{bmatrix}. \tag{2.58}$$

In fact the effect of the absorption of light in magnetic metals can by no means be neglected. In this case, the real dielectric scalar ϵ must be replaced by a complex scalar

$$\epsilon_c = \epsilon + i\frac{4\pi\sigma}{\omega}, \tag{2.59}$$

and all the other electromagnetic equations will remain identical[33]. Thus, the Voigt vector **Q** is also complex.

In some literature a complex index of refraction N is used in place of a complex dielectric constant ϵ_c:

$$N = \sqrt{\epsilon_c} = n(1 - ik) \tag{2.60}$$

where n is the real index of refraction anf k the absorption index. If we take the mirror surface to be xy-plane, the incident plane of light yz-plane, and the direction of the magnetization along y-axis, then only $Q_2 = Q$ is non-vanishing, and the dielectric tensor expression (2.58) is simplified to be

$$\epsilon = N^2 \begin{bmatrix} 1 & 0 & -iQ \\ 0 & 1 & 0 \\ iQ & 0 & 1 \end{bmatrix}. \tag{2.61}$$

W. Voigt[32] gave the first complete classical treatment of Kerr effect which was later developed whithin a broader framework by C. C. Robinson[34]. By taking into account the absorption in the metal and choosing the proper boundary conditions, the following equation which describes the reflection at a boundary between air and a magnetic metal had been obtained,

$$\begin{aligned} E_s^r &= r_{ss}E_s^i + r_{sp}E_p^i, \\ E_p^r &= r_{ps}E_s^i + r_{pp}E_p^i, \end{aligned} \tag{2.62}$$

where E_s^i and E_p^i represent the electric field components of the incident wave vibrating in the plane of the mirror surface (s) and in the plane of incidence (p), respectively, and they have the same phase, set to zero for simplicity, since the incident beam is linearly polarized. E_s^r and E_p^r are the corresponding components of the reflected wave. The reflection coefficients r_{ss} and r_{pp}, connecting the incident wave and the reflected wave in the same azimuths, are the ordinary metallic reflection coefficients given by the Fresnel equation. The reflection coefficients r_{sp} and r_{ps} provide a reflected component along the azimuth perpendicular to that of the incident wave. These are Kerr reflection coefficients that give rise to the Kerr components. Voigt derived the expression for the reflection coefficients

$$\begin{aligned} r_{ss} &= \frac{\cos\phi_i - N\cos\phi_t}{\cos\phi_i + N\cos\phi_t}, \\ r_{pp} &= \frac{N\cos\phi_i - \cos\phi_t}{N\cos\phi_i + \cos\phi_t}, \\ r_{sp} &= -r_{ps} = \frac{-iQ\cos\phi_i\sin\phi_i}{\cos\phi_t(\cos\phi_i + N\cos\phi_t)(N\cos\phi_i + \cos\phi_t)}, \end{aligned} \tag{2.63}$$

where ϕ_i and ϕ_t are the angles of incidence and refraction, respectively. It is obvious that, upon reversing the direction of the magnetization, the Voigt vector Q and therefore the Kerr reflection coefficients r_{sp} and r_{ps} change signs, and that there is a symmetrical rotation of the major axis of the elliptic polarization to the other side of the p plane. The sign of the ellipticity also reverses. The Kerr effect disappears for normal incidence on the mirror when ϕ_i=0.

Although the Kerr effect exists for any arbitrary direction of the magnetization, the longitudinal Kerr geometry (see Fig. 1.2) is the one most frequently used in magnetic measurements. In this geometry, the mgnetic metal mirror is magnetized in a direction that is parrallel both to the plane of incidence and to the surface of the mirror. The incident light beam is linearly polarized with its electric vector in the plane of incidence (i.e., the incident light is p-polarized with $E_s^i = 0$) and is reflected obliquely from the mirror. In this case, (2.62) becomes

$$\begin{aligned} E_s^r &= r_{sp}E_p^i, \\ E_p^r &= r_{pp}E_p^i. \end{aligned} \tag{2.64}$$

A p component appears in the reflected beam as in the case of an ordinary metallic reflection. In addition, because of the magnetization in the surface, a small s component appears in the reflected beam. In general, this second electric field component is out of phase with the reflected p component. Therefore, the reflected light becomes elliptically polarized with a slight rotation of the major axis of ellipse away from the p plane. These polarization changes are called the Kerr rotation and ellipticity. Upon reversing the magnetization, the Kerr component changes its sign.

Chapter 3

Experimental Methods

3.1 Magneto-Optic Kerr Effect Apparatus

3.1.1 Principle of Design

The polarization of monochromatic plane waves can be fully described by either of the two equivalent sets of parameters, θ and ϵ, or α and δ, as indicated in Fig. 2.1 and associated with each other through equations of polarimetry (2.8).

For the majority of ferromagnetic films and multilayers, the value of α, ϵ and θ are very small, say, around or less than 20'; thus, Equation (2.8) can be approximated to be

$$\begin{aligned} \theta &= \alpha \cos \delta, \\ \varepsilon &= \alpha \sin \delta \end{aligned} \tag{3.1}$$

with an inaccuracy of 0.004%.

Equation (3.1) suggests the graphical relation shown in Fig. 3.1. The point **P** represents an elliptic polarization described by θ and ϵ, or α and δ. If the ellipticity axis is made imaginary, 0P becomes the complex amplitude-rotation vector $\alpha e^{i\delta}$ with real and imaginary parts θ and $i\epsilon$.

In accordance with (2.62), the two components of the **E** vector field of the reflected beam are notated as E_p^r in the plane of incidence and E_s^r perpendicular to the palne

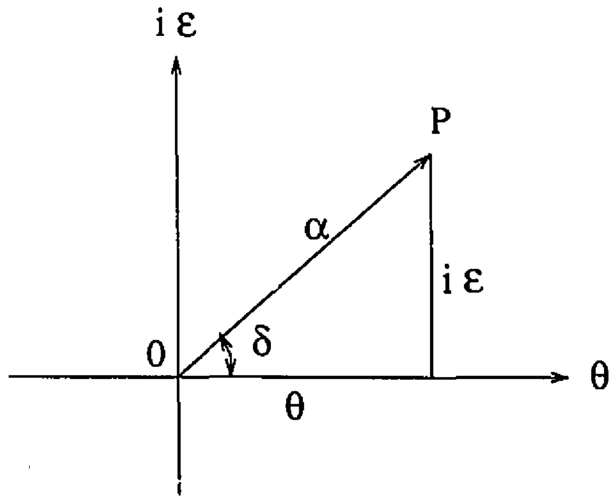

Figure 3.1: Simple graphical relation between the elliptic parameters for small values of α, ϵ and θ.

of incidence, respectively. Thus, (2.17) can be rewritten as

$$\begin{aligned} E_p^r &= a_1 e^{i\delta_1}, \\ E_s^r &= a_2 e^{i\delta_2}. \end{aligned} \tag{3.2}$$

Their ratio is

$$\frac{E_s^r}{E_p^r} = \frac{a_2}{a_1} e^{i\delta} \tag{3.3}$$

where $\delta = \delta_2 - \delta_1$.

From (2.7), we have

$$tan\ \alpha = \frac{a_2}{a_1}. \tag{3.4}$$

In the approximation of small angles, (3.3) becomes

$$\frac{E_s^r}{E_p^r} = \alpha e^{i\delta} \tag{3.5}$$

which, combining with (3.1), gives

$$\frac{E_s^r}{E_p^r} = \theta + i\varepsilon. \tag{3.6}$$

Through (3.6), MOKE experessed by (2.62) and (2.63) is therefore connected with the polarization of the reflected light which can be measured by ellipsometry.

3.1.2 Optical Layout

An apparatus has been developed to measure the Kerr rotation and ellipticity of a magnetic sample. A schematic diagram is given in Fig. 3.2.

The light source is a 6328 Å red He-Ne laser of 15 mW which is highly monochromatic, spatially and temporally coherent, and is reasonably well plane-polarized.

A Glan-Thompson polarizing prism which is mounted into a precision polarizer holder is inserted in the incident beam to improve the polarization of the laser. The holder has manual 360^0 rotation, and the precision adjustments through an extremely fine pitch lead screw can be achieved with an accuracy of 0.001^0.

The sample is mounted in an aluminium holder which has manual 360^0 rotation in the plane parallel to the magnetic field and perpendicular to the plane of incidence. The sample holder is attached to a non-magnetic kinematic-type mini mirror mount which has a total movement of 6^0 about both the horizontal and vertical axes accomplished by turning two spring-loaded precision thumb screws.

The angle of incidence is 23^0, due to the geometrical limitation of the electromagnet. A longitudinal Kerr geometry is employed. If the sample initially has zero net magnetization, then the Voigt vector $\mathbf{Q}$ vanishes, and so do the coifficients r_{sp} and r_{ps}. According to the longitudinal Kerr effect formula (2.64), the reflection beam will remain p-polarized. The reflection beam then enters the analyzer which is the same as a polarizer in structure and is adjusted to the p-polarization extinction position. Practically, it is very difficult to produce a purely p-polarized incident beam; thus, according to (2.62), a non-zero s component will occur in the reflection beam due to the ordinary metallic reflection. Fortunately, this s component does not change with the application of an external magnetic field and has no contribution to the Kerr rotation and ellipticity, so that it can be neglected in the Kerr effect analysis.

The detector assembly consists of a silicon photodiode and a large dynamic range amplifier. The amplifier is connected to the photodiode and converts current signals from the photodiode into a voltage while maintaining a constant zero bias across the detector. In the amplifier there are nine gain settings available ranging from 1 gigohm

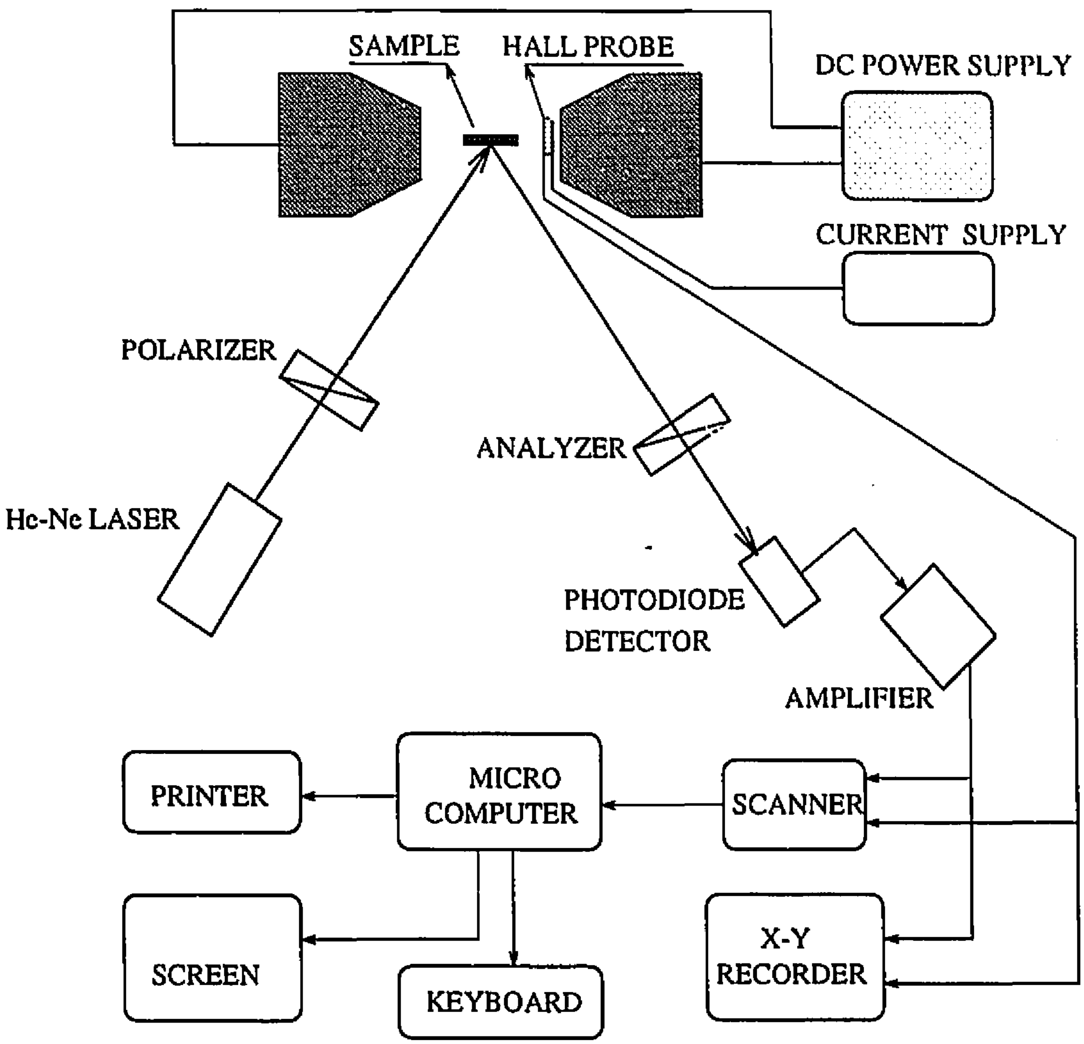

Figure 3.2: Schematical diagram of the Kerr effect apparatus.

to 10 ohms. This permits an accurate detection of signals from 1 pA to 100 mA. The amplifier has a readout window showing the photocurrent and an output which can be read by an external device.

The He-Ne laser, the polarizer, the analyzer, and the photodiode detector are supported by carriers on top of optical rails which are mounted on an optical breadboard.

All the optical devices used in this apparatus are products of Melles Griot. These optical products are listed in Table 3.1

Table 3.1: Optical products used in the Kerr effect measurement apparatus.

Optical Item	Product Number	Number of Pieces
6328 Å He-Ne Laser		1
Glan-Thompson Polarizing Prism	03PTH101	2
Precision Polarizer Holder	07HPT001	2
Kinematic-Type Mini Mirror Mount	(assemply)	1
Silicon Photodiode	13DSI001	1
Universal Modular Mount	(assemply)	1
Large Dynamic Range Amplifier	13AMP003	1
Optical Rail	07ORP003	2
	07ORP007	1
Optical Rail Carrier	07OCP501	6
	07OCP503	1
Optical Breadboard	07OBH521	1

Once the magnetic field is applied and the sample is magnetized, the reflected beam will contain an s-component E_s^r which is proportional to the magnetic field and generally not in phase with the p-component E_p^r due to the Kerr effect with $E_s^r \ll E_p^r$. The reflected beam is then elliptically polarized with the Kerr rotation θ and ellipticity ε defined in (3.6).

3.1.3 Kerr Ellipticity and Rotation vs Magnetization

In the longitudinal geometry, it is supposed that s component in the incident beam vanishes. According to (2.64) the ratio of E_s^r to E_p^r is

$$\frac{E_s^r}{E_p^r} = \frac{r_{sp}}{r_{pp}}. \tag{3.7}$$

For a magnetic medium sample described in Section 2.3, substituting (2.63) into (3.7) gives

$$\frac{E_s^r}{E_p^r} = \eta Q \tag{3.8}$$

where Q is the complex component along the direction of the applied field of the Voigt vector defined in (2.57), and η is a complex constant defined as

$$\eta \equiv \frac{-icos\phi_i sin\phi_i(Ncos\phi_i - cos\phi_t)}{cos\phi_t(cos\phi_i + Ncos\phi_t)} \tag{3.9}$$

According to (2.57), (3.8) becomes

$$\frac{E_s^r}{E_p^r} = \xi M \tag{3.10}$$

where M is the magnetization along the direction of the applied field and ξ is a complex constant defined as

$$\xi \equiv \eta f/\epsilon. \tag{3.11}$$

From (3.6) and (3.10) we get the relation between the Kerr ellipticity and rotation vs the magnetization

$$M = \frac{\varepsilon}{\xi}(\frac{\theta}{\varepsilon} + i). \tag{3.12}$$

3.1.4 Kerr Ellipticity and Rotation vs Kerr Intensity

Practically, we set the analyzer a small angle β from extinction under the zero net magnetization as shown in Fig. 3.3.

A photodiode is a quantum device, and the current output from it is proportinal to the photo detection rate, i.e., to the power of the the signals detected by it.

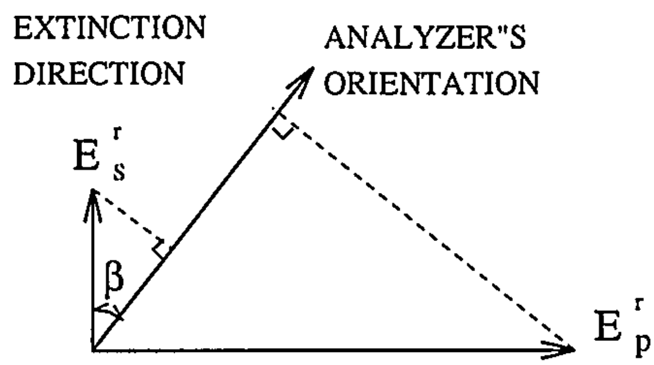

Figure 3.3: The analyzer's actual orientation. The extinction orientation is perpendicular to the p direction. E_s^r shows up with the net non-zero magnetization of the sample.

Classically, the photogenerated current I, hereafter named *the Kerr intensity*, can be expressed as

$$I = \mid iE_p^r sin\,\beta + E_s^r cos\,\beta \mid^2 \tag{3.13}$$

which has the approximation form for small β

$$\begin{aligned} I = & \mid iE_p^r\beta + E_s^r \mid^2 \\ = & \mid E_p^r \mid^2 \mid \beta \mid^2 \mid i + \frac{1}{\beta}\frac{E_s^r}{E_p^r} \mid^2 . \end{aligned} \tag{3.14}$$

Substituting (3.6) into (3.14) results in

$$\begin{aligned} I = & I_0 \mid i + \tfrac{1}{\beta}(\theta + i\varepsilon) \mid^2 \\ = & I_0[(\tfrac{\theta}{\beta})^2 + (1 + \tfrac{\varepsilon}{\beta})^2], \end{aligned} \tag{3.15}$$

where $I_0 \equiv \mid E_p^r \mid^2 \mid \beta \mid^2$ is the Kerr intensity at zero net magnetization.

On the other hand, θ/β and ε/β are very small. Let θ and ϵ be 20' and β be fixed at 2^0. If we neglect the squred terms of θ/β and ε/β in (3.15), then the inaccuracy is less than 1%; in this case, (3.15) reduces to be

$$I = I_0(1 + \frac{2\varepsilon}{\beta}). \tag{3.16}$$

The Kerr ellipticity ε can be expressed in terms of the Kerr intensity,

$$\varepsilon = \frac{\beta}{2}\frac{I - I_0}{I_0}. \tag{3.17}$$

From (3.12) and (3.17) we know that, once normalized, hysteresis loops of the magnetization, the Kerr ellipticity and the Kerr intensity are the same, i. e.,

$$M \sim \varepsilon \sim I - I_0. \tag{3.18}$$

3.1.5 Data Aquisition System

In Section 3.1.3, we have established a theoretical model and the concerned adjustment methods which combine to result in the Kerr rotation and ellipticity in terms of the Kerr intensity. To get the Kerr hysteresis loop, we need to connect the Kerr ellipticity with the variation of magnetic fields.

A Hall effect probe is placed on one pole of the magnet to monitor the magnetic field. A standard Gaussmeter has been employed to calibrate the Hall voltage with the actual value of field. The calibration curve is shown in Fig. 3.4.

It can be seen that a nearly-perfect linear relation exists between the Hall voltage and the field with a constant of 10.13 mV/kOe.

A computer-aided data aquisition system has been developed to measure the Kerr hysteresis loops. A Keithley mode 199 system DMM scanner is used to read the detector output and the Hall voltage, and a built-in A/D converter converts those analog signals into digital signals. Using a data aquisition program written in C language, a microcomputer reads the Kerr intensity and Hall voltage.

In place of the computer-aided data aquisition system, a much simpler X-Y recorder is a good alternative with the advantage of fast measurement and satisfactory accuracy, but reduces the ease of data transfer and processing.

3.1.6 Improvement of Techniques

The optical layout and detecting assembly are extremely sensitive to optical, mechanical and electrical interference from the surroundings. During the set-up of the

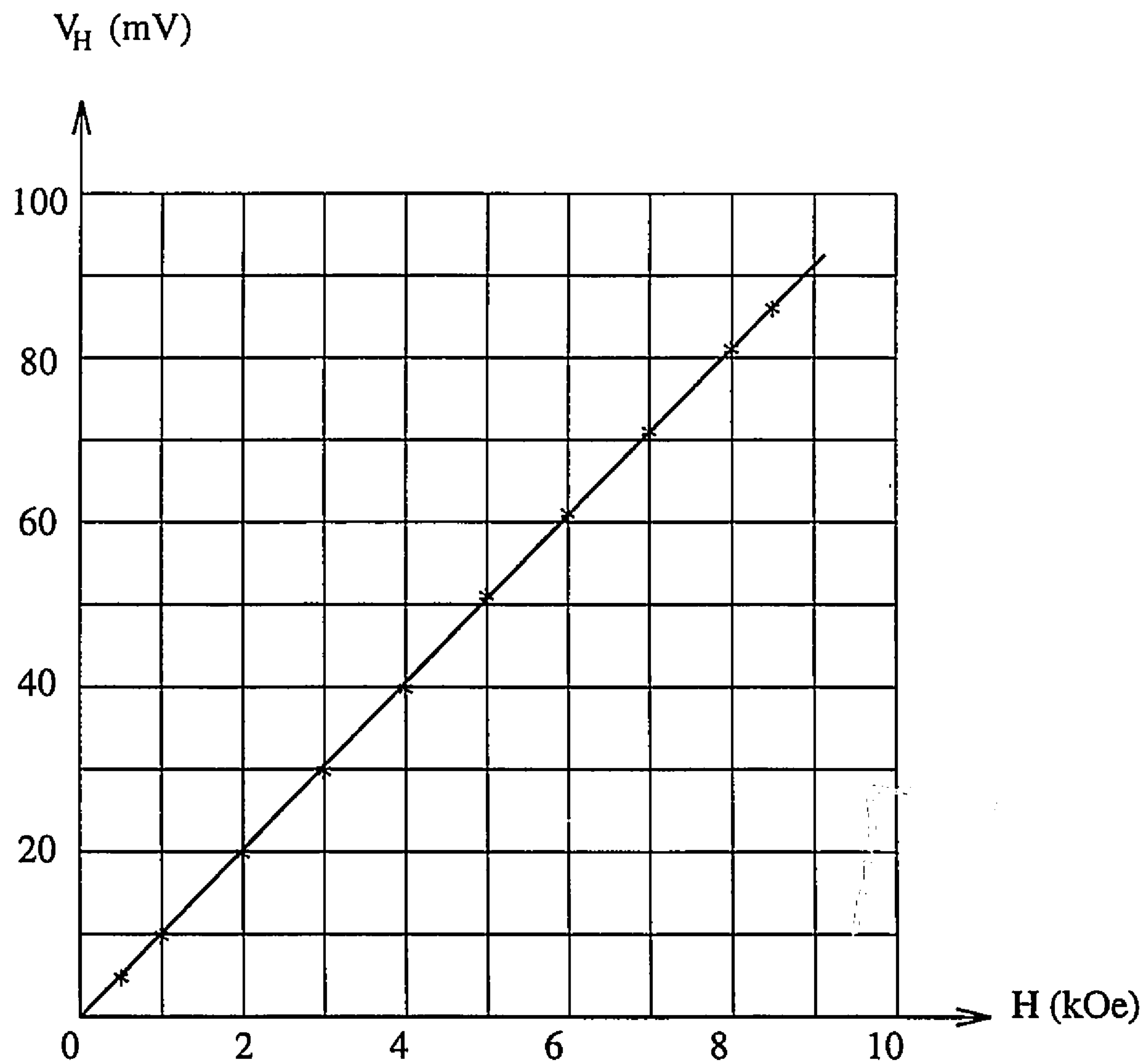

Figure 3.4: Calibration curve of voltage values from the Hall effect probe with standard magnetic field.

apparatus, we have identified most sources of signal noise and drift, and reduced these to a minimum. In order to optimize the experimental results, the following procedures have been adopted:

1) The sample is screwed to its holder through a tiny copper plate. The screws must be tight enough to keep the sample firm, but can not be so tight that a stress develops in the sample.

2) A black paper tube of 6 cm in length and 3.5 cm in diameter is used to shield the optical path between the analyzer and the photodiode detector from randomly scattered light.

3) Irrelevant electric wires are kept far away from the photodiode, which can reduce the noise level significantly.

4) In principle, the analyzer could be set to the extinction position at which detected signals would be minimum at net zero magnetization. However, such a net zero magnetization is hard to locate for ferromagnetic samples. Instead, the approach of two subminima has been used. The two minima points are obtained at two saturation magnetic fields of opposite directions. The actual minimum is then obtained by averaging the data pair.

Fig. 3.5 gives an example of the longitudinal Kerr intensity measurement using this apparatus. The sample is a 1000 Å sputtered Co film. A satuation field of 110 Oe is observed.

3.1.7 Improvement of Apparatus

I. Measurement of Transverse MOKE

We can measure the transverse magneto-optic Kerr effect if we insert a half-wave plate before the polarizer to rotate the **E** vector of the incident beam perpendicular to the incident plane, i.e., the incident beam is s-polarized. The following polarizer can be adjusted to maintain a relatively pure s-polarization in the incident beam.

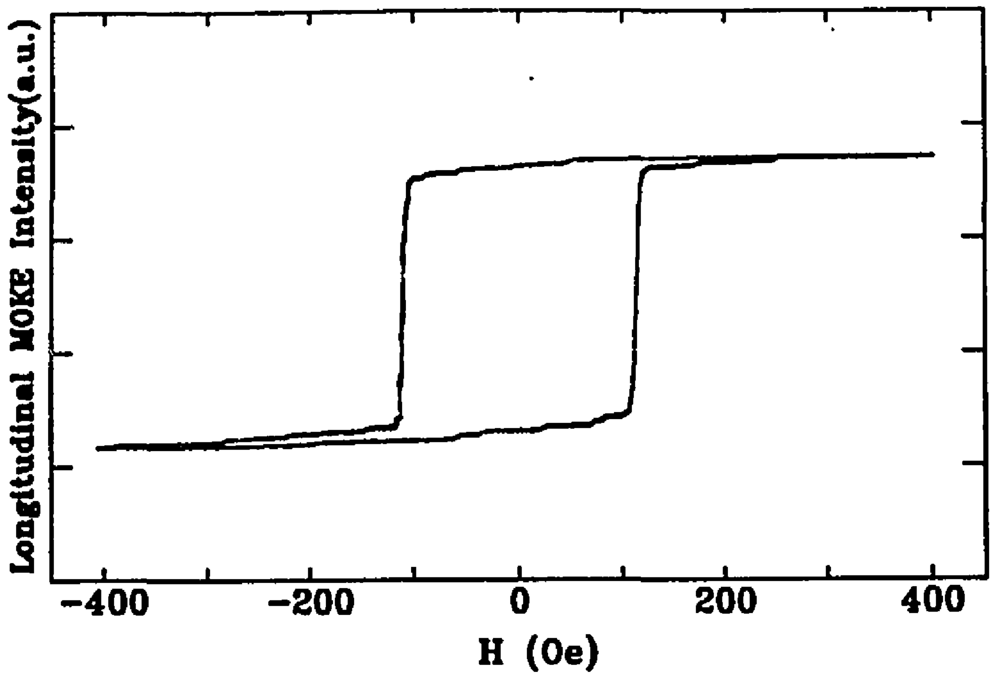

Figure 3.5: Longitudinal magneto-optic Kerr hysteresis of a 1000 Å sputtered Co film.

II. Measurement of Polar MOKE

This apparatus can be converted to measure the polar magneto-optic Kerr effect by inserting a nonmagnetic metal mirrior of high reflection as shown in Fig. 3.6. The sample is placed with its mirror suface perpendicular to the magnetic fields and reflects the beam backward onto the metal mirror's surface. The beam is then reflected into the analyzer outside the magnet. The reflection from the metal mirror will introduce into the beam a minute elliptic polarization due to the ordinary metallic reflection. We should balance the adjustment of the polarizer, the analyzer, the mirrior and the sample to achieve detectable signals. Fig. 3.7 gives the polar Kerr intensity measurement on the same 1000 Å sputtered Co film as that used in the longitudinal MOKE measurement. The satuation field is 550 Oe, five times as large as before. This is due to the fact the shape anisotropy in such a 1000 Å Co film results in a hard magnetization axis along the perpendicular direction.

Finally, it should be mentioned that the spectroscopic MOKE, a technique used in

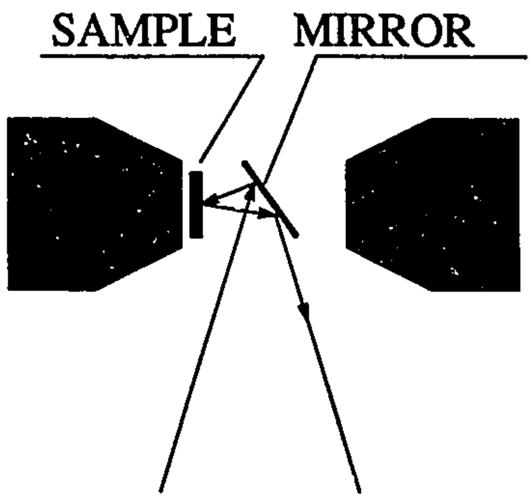

Figure 3.6: Arrangement for the polar MOKE measurement

research of magneto-optic memory materials, can be measured if the laser is replaced with a monochrometer and an arc lamp.

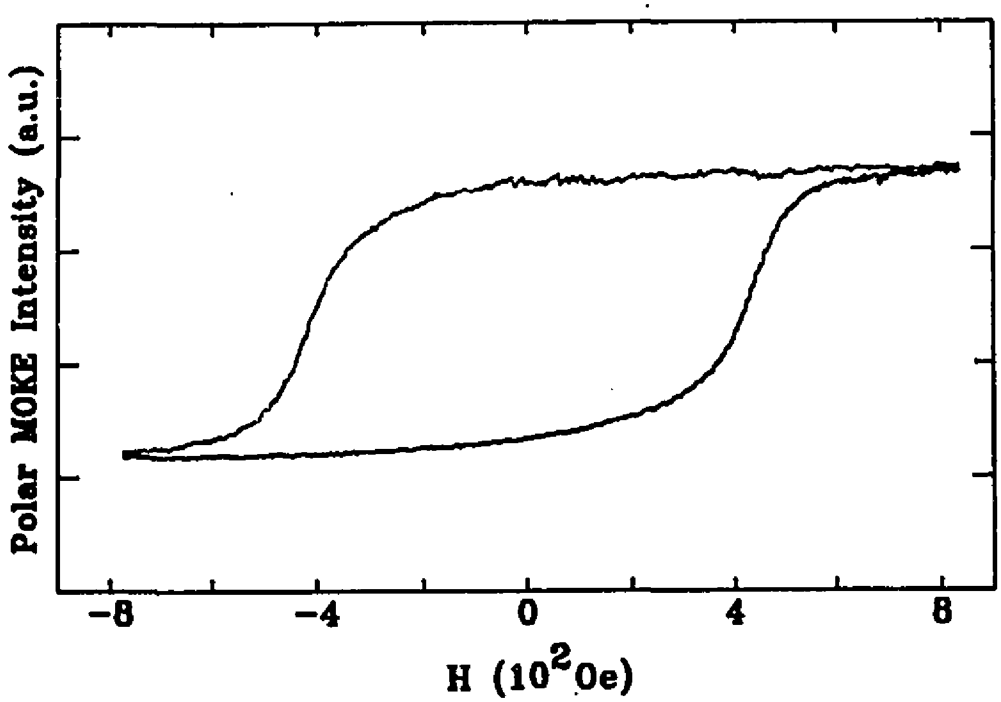

Figure 3.7: Polar magneto-optic Kerr hysteresis of a 1000 Å sputtered Co film.

3.2 Preparation of Multilayers by Sputtering

A wide variety of film deposition techniques have been used for the preparation of multilayers. Sputtering is notable for the ease with which many different materials can be deposited at relatively high deposition rates. This method uses a *dc* glow discharge between the plate of source material and the substrate upon which the film is deposited. A summary of the physics of glow discharge processes can be found in the literature[35]. Fig. 3.8 shows the schematic diagram of our two-source sputtering apparatus.

The source material is machined into a cylinder of 25 mm in diameter and 2 ~ 3 mm thick in order to fit the suource holder. Before sputtering, the chamber must be evacuated. Upon the application of electric field the sputtering gas (Ar in this case) is ionized and Ar^+ ions bombard the source material. If the kinetic energy of Ar^+

ions exceed roughly four times the heat of sublimation of the source material, atoms are knocked off the source and ejected into the gas phase whence they are deposited on the substrate. However the energy of these ejected atoms will be reduced by collisions with the sputtering gas prior to deposition on the substrate. The collision process depends on a variety of factors including the sputtering gas pressure and the construction of the chamber, e. g., the source-substrate distance. In our sputtering apparatus, the deposition rate is adjusted by changing the sputtering gas pressure.

The source holders are designed associated with magnetrons which consist of strong permenent magnets and give rise to a magnetic field which confines the plasma close to the source material and away from the substrate. This reduces damage to the substrate and the deposited film from energetic ion bombardment. This also allows the use of lower sputtering gas pressure while maitaining relatively high growth rates. The concentration of impurities in the deposited film from residual gases in the system, such as oxygen or nitrogen, depends on the film growth rate versus the residual gas pressures in the deposition system. Thus magnetron sputtering deposition leads to films with low residual gas impurity level.

The rotation of the substrate plate is controlled by a microcomputer. Multilayers of fixed layer thickness and layer number can be obtained by setting corresponding parameters in the control program[36].

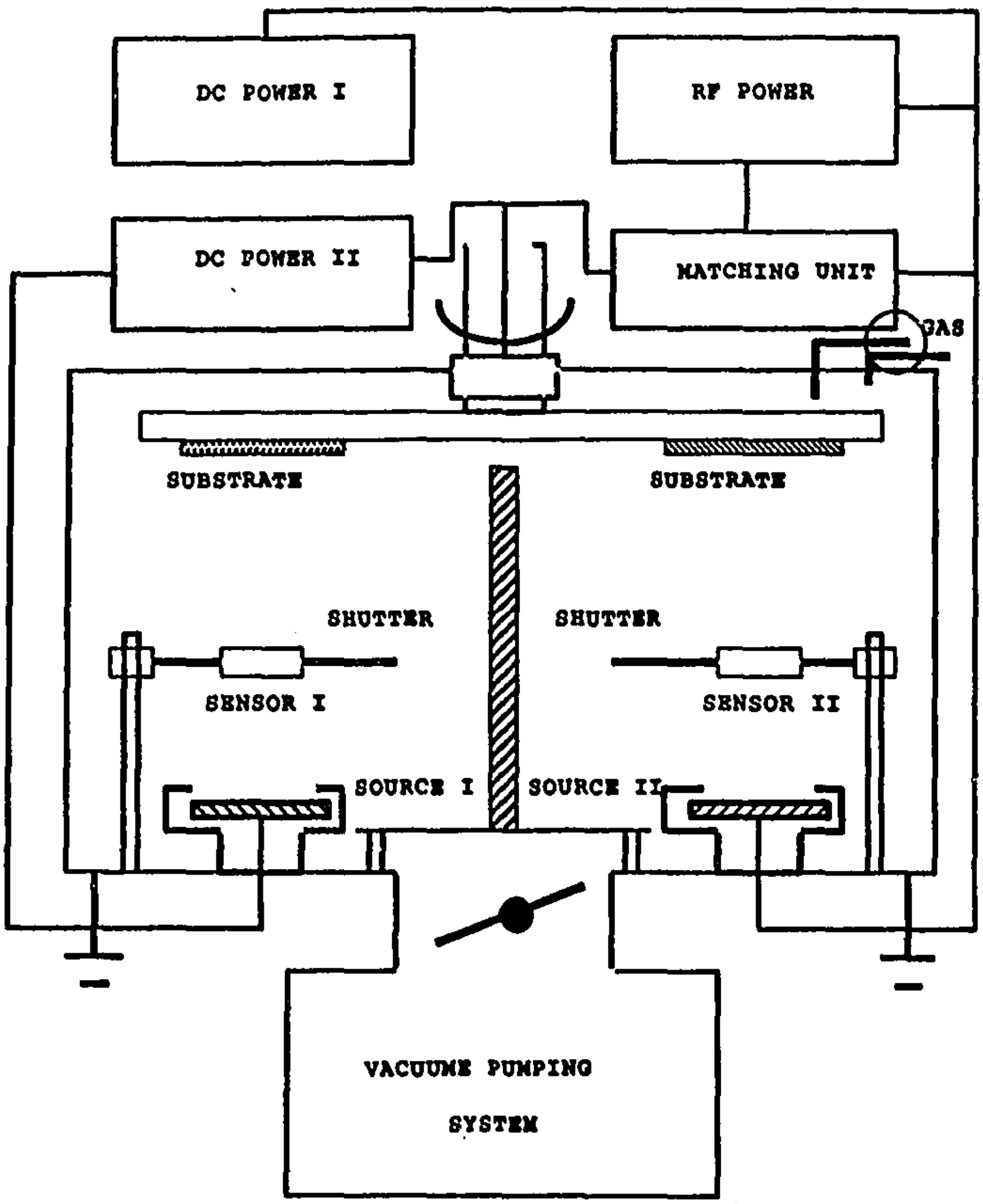

Figure 3.8: Schematic Diagram of Sputtering Apparatus

3.3 Structural Characterization by X-Ray Diffraction

The physical properties of multilayers depend strongly on the atomic structure of individual layers and the superlattice structure. A structural examination is a very important step toward understanding the magnetic and transport properties of magnetic multilayers. X-ray diffraction is widely used to characterize the structure of multilayers[37]. Detailed structural information can be obtained by modeling multilayer structures and comparing their calculated x-ray intensity with the experimental data[38,39].

The most commonly used x-ray scattering geometry is the reflection geometry in which the scattering vector is normal to the film. Reflectivity measurements are conventionally separated between the low-angle ($< 20^0$) and high-angle ($> 20^0$) regions of the spectra.

In the low-angle region, the length scales studied are greater than the lattice spacings of the constituent layers, so the scattering can be considered as arising solely from the chemical modulation of the structure[40].

Low-angle x-ray reflectivity experiments were performed using a high-resulotion triple-axis diffractometer with a Cu-Kα sealed tube shown schematically in Fig. 3.9[41]. By using a single-crystal Ge (111) monochrometer and analyzer, a resolution of order 0.01^0, full width at half maximum (FWHM), for a $\theta - 2\theta$ scan was achieved, corresponding to a ΔQ of 0.0004 $\AA^{-1}$ (FWHM) in reciprocal space. The original x-ray beam dimension of 1×4 mm^2 was reduced by slit # 3 to 0.4 mm in the vertical direction (in the plane of scattering) and 2.0 mm in horizontal direction. Slit # 4 is actually the acceptance window in the analyzer housing. The maximum beam density at zero 2θ with no sample present (where θ is the beam incident angle) is about 220,000 cps with the tube power setting at 40 kV$\times$40 mA. The sample was fixed in a holder whose rotation in the plane perpendicular to the sample's surface was controlled by a microcomputer. The initial alignment procedure was for the sample to block half the Kα_1 x-ray beam at θ=0. The blocking was checked by ω scan around θ=0. Since the low-angle reflectivity is very sensitive to the alignment of the sample and the diffractometer, extreme care was taken in order to maintain the same alignment conditions for all the samples. After complete aligning of the the sample, a $\theta - 2\theta$ scan was taken to measure the specular reflection signal.

High-angle x-ray diffraction measurments were carried out on a conventional powder diffractometer with Cu-Kα radiation. The instrumental broadening for this diffractometer was estimated to be 0.15^0 FWHM for a $\theta - 2\theta$ scan.

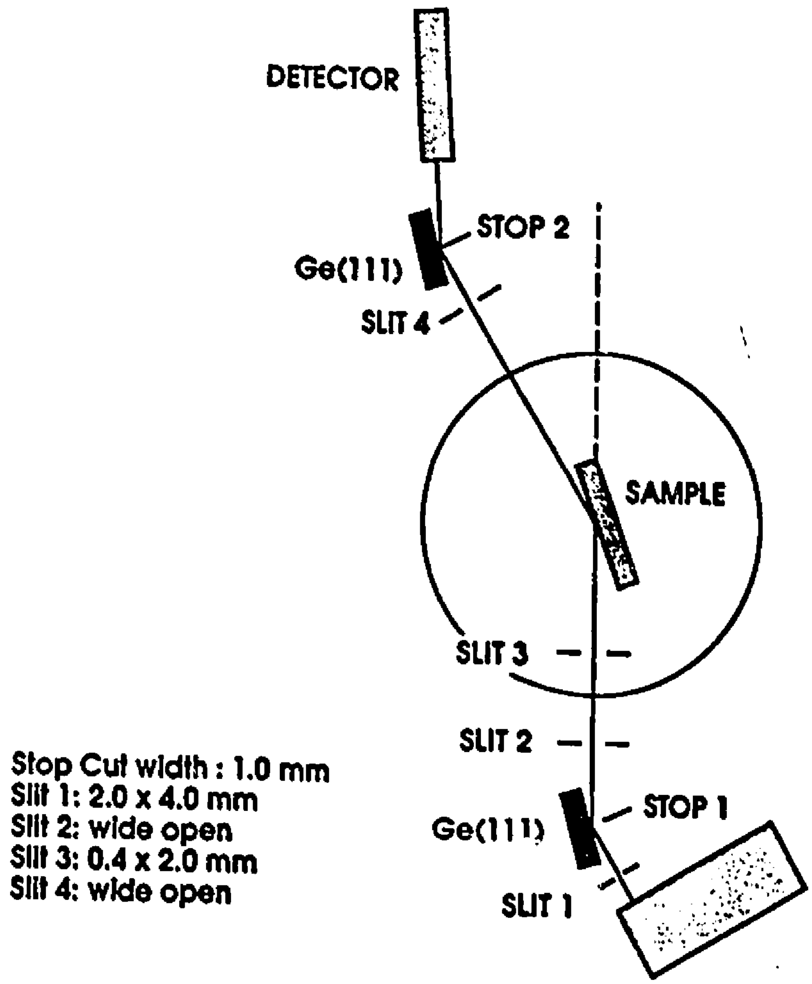

Figure 3.9: Triple-axis x-ray diffractometer with high-resolution setup.

3.4 Magnetotransport Measurements

Studies on magnetotransport properties (that is, properties relating to electrical conductivity in the presence of an applied magnetic field) of multilayers are very important both for fundamental understanding and for practical application. In this research, MR was measured using a microcomputer controlled high-resolution *ac* bridge in Départment de Physique, Université de Montréal[42].

The principle of MR measurement has been detailed in literature[20]. The sample dimension and geometries for the measurement are illustrated in Fig. 3.10. Sample dimension have been defined by sputtering through a mask 4 mm wide with two small arms on each side for electrical contacts distanced 8 mm apart[43]. The electric current flows in the sample plane between contacts 1 and 2. The MR was measured between contacts 3 and 4 with the magnetic field in the film plane and perpendicular to the current direction. The field is provided by the electromagnet and varied from – 1 Tesla to 1 Tesla.

Silicon vacuum grease was used to establish thermal contact between the sample holder and samples. Electrical contacts between samples and leads are secured using silver paste.

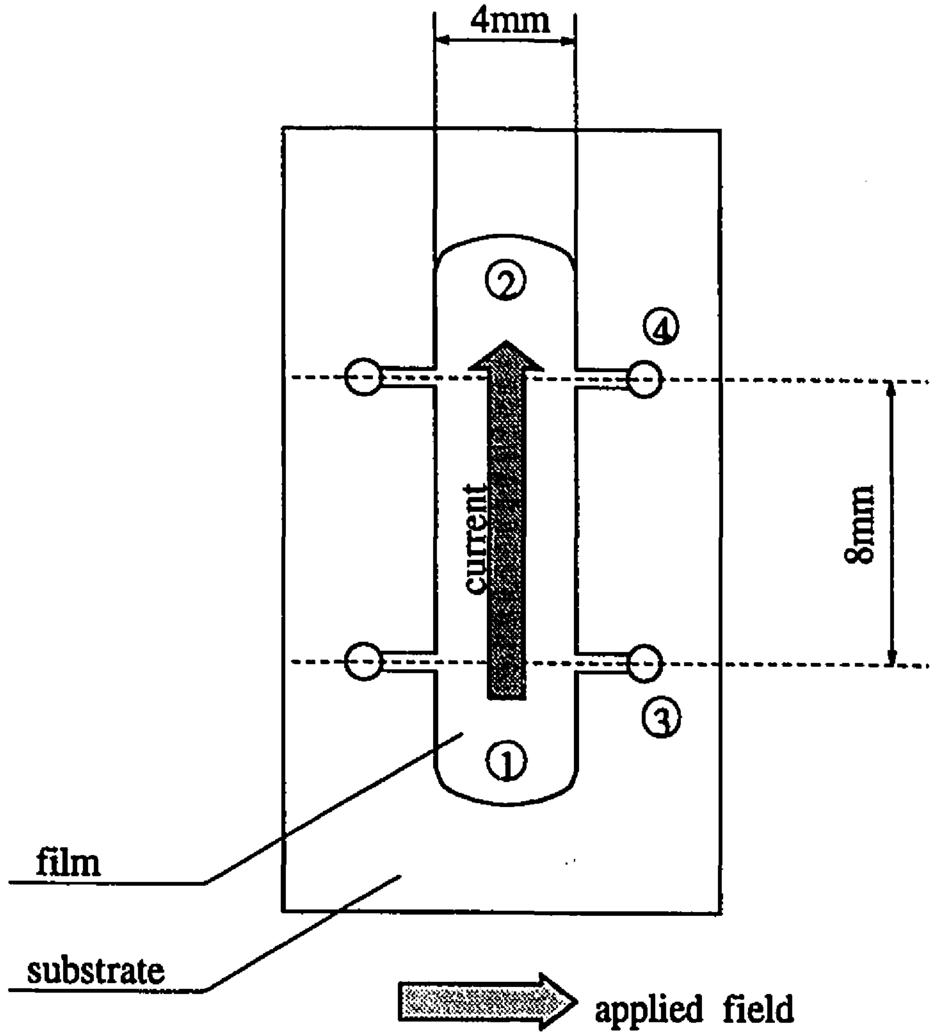

Figure 3.10: Sample dimensions and geometries for MR measurements.

Chapter 4

Experimental Results and Discussion

4.1 SMOKE of Magnetic Multilayers

Much theoretical and experimental effort has been devoted to the Kerr effect of magnetic films and multilayers[34,44–54]. The complexity arises from the fact that the light beam will be reflected from and transmit through many mangnetic and non-magnetic layers before it is fully absorbed. Therefore, both Faraday and Kerr magneto-optic effects will be involved in the radiation reflected from a magnetic multilayer, though it is still conventionally named Kerr effect for its reflection characteristics.

We will follow the description by Zak, *et al* [53], and consider a multilayer with the surface parallel to the xy-plane. In each magnetic layer the dielectric tensor takes the form of (2.58). The goal is still to find the relation between the electric field of incidence, represented by (E^i_s, E^i_p), and that of reflection, (E^r_s, E^r_p), on the surface of the multilayer. The boundary condition requires that:

1) at each interface of the superlattice, the tangential components of the electric field (E_x, E_y) and magnetic filed (H_x, H_y) are continuous. In defining the magneto-optic coefficients the quantitities E^i_s, E^i_p, E^r_s *and* E^r_p shown in Fig. 4.1 will be used

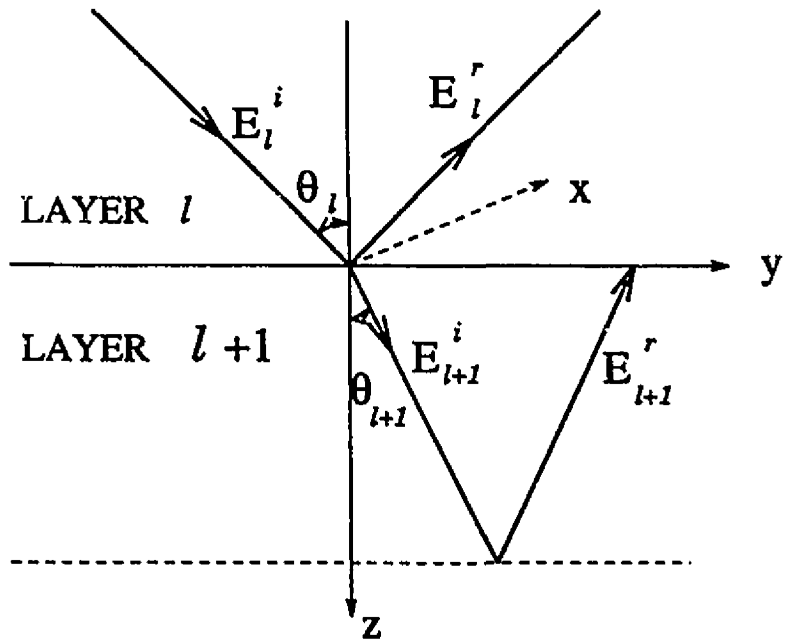

Figure 4.1: A boundary between layers. The xy-plane is the boundary between media l and l+1. Waves going in the z-direction are denoted by $\mathbf{E}^i$, while those opposite to the z-direction are $\mathbf{E}^r$. θ_l and θ_{l+1} are the angles in the Snell's law.

with the subscripts s and p taking their usual meaning.

2) the light will be totally absorbed in the substrate and no reflected component will be present, thus in the last layer adjacent the substrate we have

$$(E_s^i, E_p^i, E_s^r, E_p^r) = (E_s^t, E_p^t, 0, 0) \tag{4.1}$$

where E_s^t and E_p^t are the electric fields transmitted through the layer.

Formally, we can relate (E_s^i, E_p^i, E_s^r, E_p^r) with (E_x, E_y, H_x, H_y) within each layer of the superlattice, and (E_s^i, E_p^i, E_s^r, E_p^r) at lth interface with (E_s^i, E_p^i, E_s^r, E_p^r) at (l+1)th interface using two types of 4×4 matrices, A and D, referred to as the *medium* *boundary* and *medium propagation matrices* as follows:

$$\begin{bmatrix} E_x \\ E_y \\ H_x \\ H_y \end{bmatrix}_l = A_l \begin{bmatrix} E_s^i \\ E_p^i \\ E_s^r \\ E_p^r \end{bmatrix}_l \tag{4.2}$$

and

$$\begin{bmatrix} E_s^i \\ E_p^i \\ E_s^r \\ E_p^r \end{bmatrix}_l = D_l \begin{bmatrix} E_s^i \\ E_p^i \\ E_s^r \\ E_p^r \end{bmatrix}_{l+1} \tag{4.3}$$

The boundary condition of continuity at each interface then is given by

$$A_i \begin{bmatrix} E_x \\ E_y \\ H_x \\ H_y \end{bmatrix} = \Pi(A_l D_l A_l^{-1}) A_f \begin{bmatrix} E_s^t \\ E_p^t \\ 0 \\ 0 \end{bmatrix}. \tag{4.4}$$

Here the subscripts of i and f stand for the initial and final materials. The matrix elements of A and D are constructed from the geometric angles of the problem and from the N and Q values of each layer. Prescriptions for constructing A and D appear in ref.[53]. After evaluating A and D matrices one can calculate the Kerr rotation and ellipticity.

In thin-film limit, where the total thickness of the multilayer is much less than the wavelenth of the incident light, the calculation of the product of those matrices in (4.4) can be greatly simplified[53]. For the longitudinal case, the result is

$$\frac{E_s^r}{E_p^r} = \frac{4\pi}{\lambda} \frac{sin\,\phi\, N_i^2 N_f}{N_i + N_f} \sum_m d_m Q_m, \tag{4.5}$$

where ϕ is the angle of incidence upon the surface of a multilayer, and N_i and N_f are indices of reflection in the initial and the final medium, respectively. The summation runs only over the thickness and the magnitude of the **Q** vector of the mth magnetic layer. The above equation gives the formulus for the *longitudinal surface magneto-optic Kerr effect* (SMOKE) of magnetic multilayers within the thin-film limit, from which we conclude that

1) SMOKE depends linearly on the thickness of the magnetic component; and

2) SMOKE is independent of the intervening nonmagnetic layers.

This theoretical prediction has been confirmed recently by experiments by Qiu, *et al.* [54].

The SMOKE is proportional to the thickness of the sum of magnetic layers, as in the case of magneto-optic Faraday effect, in a contrast to the magneto-optic Kerr effect (MOKE) of the mirror surface of a bulk magnetic medium which is independent of the thickness. In this important respect SMOKE is distinct from MOKE.

Although derived from a thin-film limit, (4.5) is valid for the majority of multilayers for the fact that, due to the absorption of light in metals, the optical penetration depth into metallic multilayers is about 100 to 200 Å which still falls into the thin-film region comparing with the optic wavelenth, e. g., 6328 Å for He-Ne laser. Thus, we are allowed to take SMOKE as a magnetic measurement of the top few layers.

From (2.29), we have

$$\mathbf{Q} = \frac{\mathbf{g}}{\epsilon} = \frac{f}{\epsilon}\mathbf{M}. \tag{4.6}$$

Then (4.5) becomes

$$\frac{E_s^r}{E_p^r} = \frac{4\pi}{\lambda}\frac{\sin\phi\, N_i^2 N_f}{N_i + N_f}\frac{f}{\epsilon}\sum_m d_m M_m \tag{4.7}$$

where M_m is the magnetization of the mth magnetic layer.

The averaged magnetization of the magnetic multilayer is notated as M with

$$M = \frac{\sum_m d_m M_m}{\sum_m d_m}. \tag{4.8}$$

With all physical and geometrical coefficients in (4.7) being absorbed into one coefficient γ,

$$\gamma \equiv \frac{4\pi}{\lambda}\frac{\sin\phi N_i^2 N_f}{N_i + N_f}\frac{f}{\epsilon}\sum_m d_m \tag{4.9}$$

which is a complex constant for given media and experimental layout, (4.7) becomes

$$\frac{E_s^r}{E_p^r} = \gamma M. \tag{4.10}$$

Through (3.6) and (4.10), the average magnetization of multilayer films is related to the Kerr rotation θ and the Ker ellipticity ε, which can be measured with the Kerr effect apparatus described in Section 3.,

$$M = \frac{1}{\gamma}(\theta + i\varepsilon). \tag{4.11}$$

Therefore, by measuring either θ or ε as a function of the applied field, we get the SMOKE hysteresis of the magnetic mutilayer films, which can be viewed as a measurement of magnetization hysteresis.

4.2 Oscillatory Interlayer Coupling in $Ni_{80}Co_{20}/Cu$ Multilayers

The interlayer coupling between magnetic layers separated by non-magnetic layers in multilayers has been measured by a variety of techniques such as neutron diffraction, spin-polarized electron scattering, scanning electron microscopy with polarization analysis, Brillouin light scattering, ferromagnetic resonance, and SMOKE. Among them, SMOKE is valued for its elegance and high resolution. It is virtually a magnetization measurement of the top few layers within the optic penetration depth at a particular location in the multilayer sample. By measuring the magnetization of multilayers as a function of an applied magnetic field — that is, by measuring the magnetization hysteresis loop — one obtains direct information on the coupling between various ferromagnetic layers. These loops can be obtained for a variety of structural and compositional parameters, in particular as a function of the thickness of the non-magnetic spacer metals.

It has been reported recently that sputtered $Ni_{80}Co_{20}/Cu$ multilayers show a well-defined oscillation of the saturation MR as a function of Cu spacer thickness[25]. We have made SMOKE measurements on these $Ni_{80}Co_{20}/Cu$ multilayer samples. Magnetization versus in-plane field loops are shown in Fig. 4.2 for a selected series of sputttered $Ni_{80}Co_{20}/Cu$ samples as a function of Cu spacer layer thickness.

The loops clearly show an oscillatory variation of saturation field H_s with Cu thickness. A detailed dependence of saturation field on Cu thickness is shown in Fig. 4.3. Three oscillatory peaks at 8 Å, 20 Å and 35 Å are observed with relatively large saturation fields, which indicates strong AF couplings, while with Cu thickness at 6 Å, 10 Å and 25 Å, ferromagnetic coupling dominates.

It is interesting to see that the GMR can be observed in an AF-coupled multilayer. In an AF-coupled multilayer, the magnetic layers have succesive antiparallel orientation. With the application of sufficient in-plane magnetic field, the exchange interaction can be overwhelmed and the magnetization of all the magnetic layers be-

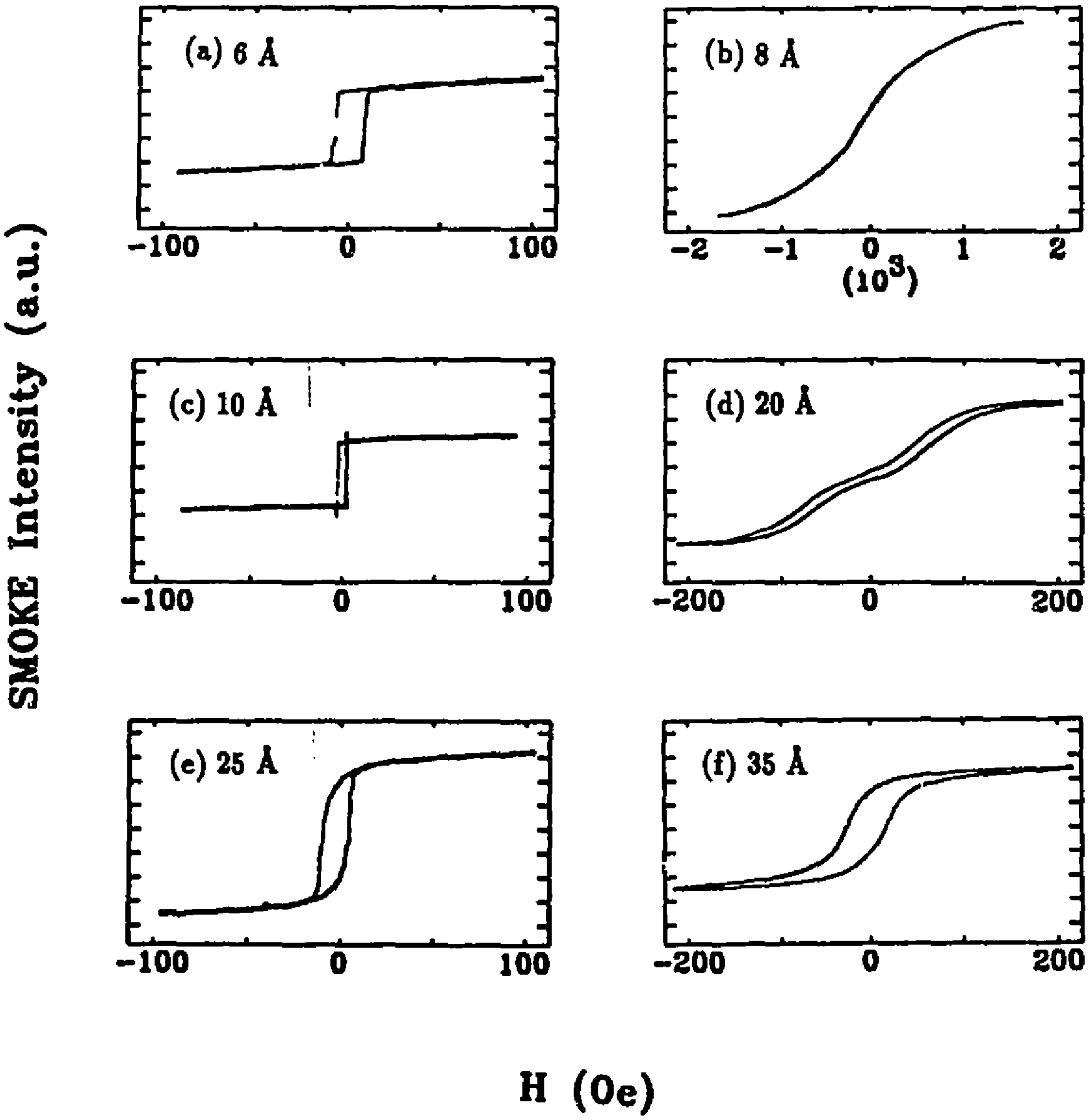

Figure 4.2: SMOKE hysteresis loops for a series of samples ($Ni_{80}Co_{20}$15Å/Cu tÅ)×30 with Cu spacer layer thickness equals (a) 6 Å; (b) 8 Å; (c) 10 Å; (d) 20 Å; (e) 25 Å; and (f) 35 Å, respectively.

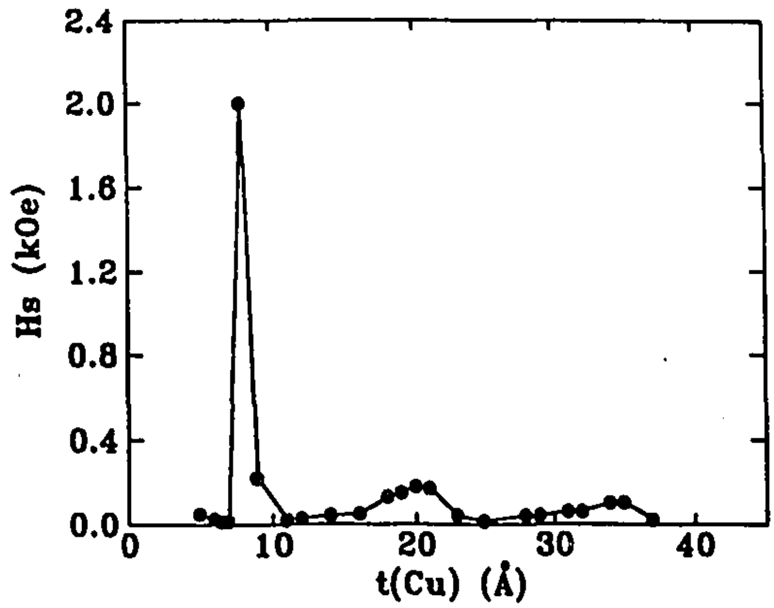

Figure 4.3: Dependences of saturation field H_s, obtained from SMOKE measurement, on Cu spacer layer thickness t(Cu) for a series of samples ($Ni_{80}Co_{20}$15Å/Cu tÅ)× 30.

comes parallel. The resistance to passage of electrons through the multilayer stack is less for the parallel configuration than for the antiparallel configuration, and this difference accounts for the GMR[55]. Fig. 4.4 shows two typical cases of MR versus applied field in an AF-coupled sample ($Ni_{80}Co_{20}$15Å/Cu20Å)× 30 and a ferromagnetically coupled sample ($Ni_{80}Co_{20}$15Å/Cu10Å)× 30.

For comparison the oscillatory variation of the saturation MR with Cu spacer thicknesses for $Ni_{80}Co_{20}$/Cu multilayers is shown in Fig. 4.5. It is found that the saturation field and the saturation MR oscillations possess the same period.

Relative strengthes of AF coupling can be derived from SMOKE hysteresis loops. As shown in Fig. 4.3 (b), the AF coupling of the $Ni_{80}Co_{20}$ layers results in a nearly net zero magnetic moment in small magnetic fields. However, the application of a magnetic field sufficiently large to overcome the AF coupling causes the magnetic moments of the $Ni_{80}Co_{20}$ layers to become aligned with the field. Consider any pair of neighboring $Ni_{80}Co_{20}$ layers in which the magnetic moments, M_1 and M_2 of the

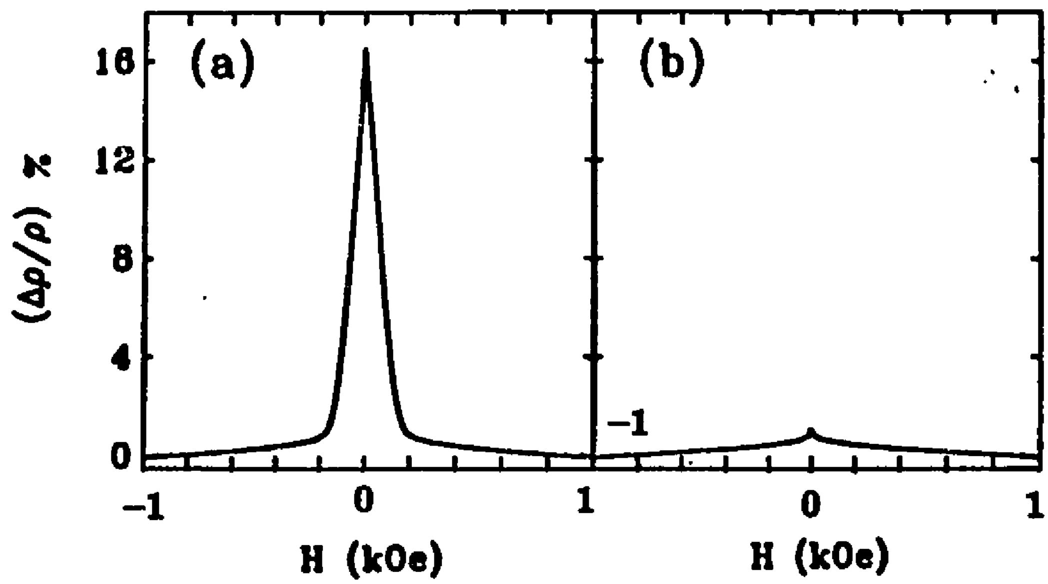

Figure 4.4: Magnetoresistances $[\Delta\rho/\rho = (\rho_0 - \rho(H_s))/\rho(H_s)]$ vs applied magnetic field at room temperature for (a) AF-coupled sample ($Ni_{80}Co_{20}$15Å/Cu20Å)× 30; and (b) ferromagnetically coupled sample ($Ni_{80}Co_{20}$15Å/Cu10Å)× 30.

$Ni_{80}Co_{20}$ layers are coupled with an interlayer exchange constant, J_{12}. The exchange coupling energy between two neighboring $Ni_{80}Co_{20}$ layers can then be written, within a Heisenberg model, as

$$E = J_{12} cos\ \theta_{12}, \tag{4.12}$$

where θ_{12} is the angle between M_1 and M_2.

In general the magnetization mechanism is rather complicated. It involves nucleation of domains, motion of domain walls and, in the case of an AF-coupled multilayer system, coherent rotation of magnetizations of adjacent magnetic layers. For an AF-coupling-dominated multilayer system, we consider the 'single-domain limit' where only coherent in-plane rotation of magnetizations is considered.

In a magnetic field, ignoring any magnetic anisotropy, the total energy of an AF-coupled multilayer per unit area is

$$E(H) = 2J_{12} cos\ (\phi_1 - \phi_2) - M_s t_M H(cos\ \phi_1 + cos\ \phi_2) \tag{4.13}$$

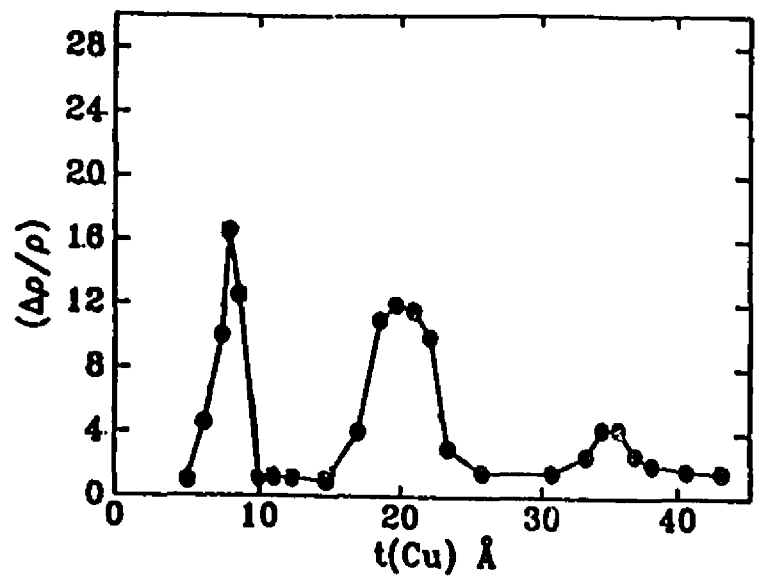

Figure 4.5: Dependences of MR on Cu spacer layer thickness t(Cu) for a series of samples Si/$Ni_{80}Co_{20}$50Å($Ni_{80}Co_{20}$15Å/CutÅ)×30.

where M_s is the magnetization of the $Ni_{80}Co_{20}$ layers, t_M is the thickness of each $Ni_{80}Co_{20}$ layer, ϕ_1 and ϕ_2 are the angles between H and the magnetization, as shown in Fig. 4.6, and the factor 2 before J_{12} enters because each magnetic layer interacts with its two neighboring magnetic layers.

The stable configuration of magnetizations of adjacent magnetic layers is found by minimizing the total energy, i.e., equating $\partial E/\partial\phi_1$ and ∂ E/$\partial\phi_2$ to zero, which gives, respectively,

$$-2J_{12}sin\,(\phi_1-\phi_2)-M_sHt_M\;sin\,\phi_1=0; \tag{4.14}$$

and

$$2J_{12}sin\,(\phi_1-\phi_2)-M_sHt_M\;sin\,\phi_2=0. \tag{4.15}$$

Combining the above two equations gives

$$sin\,\phi_1=-sin\,\phi_2. \tag{4.16}$$

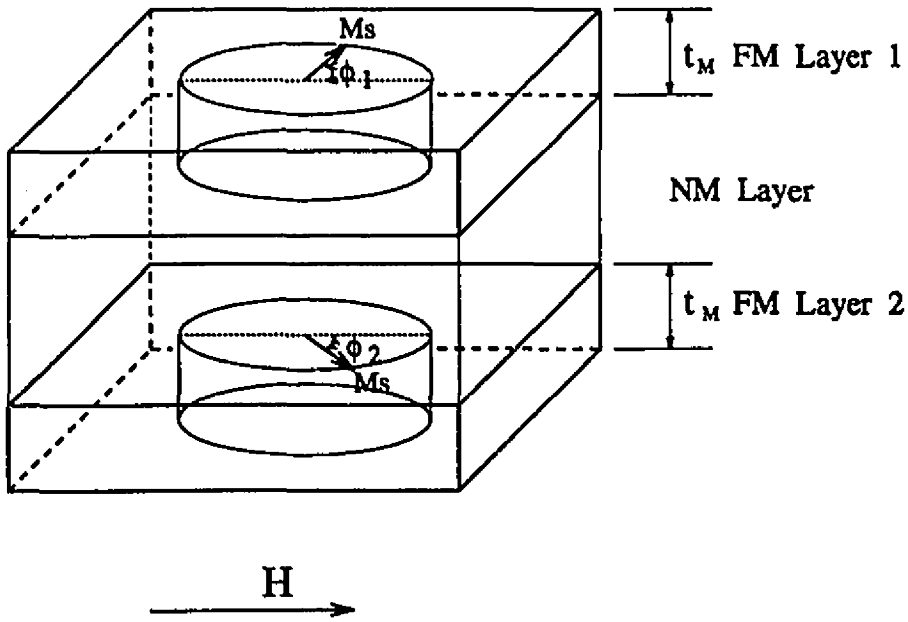

Figure 4.6: Definition illustration of M_s, t_M, ϕ_1 and ϕ_2 in an AF-coupled multilayered system.

The smooth magnetization process suggests one solution to (4.16),

$$\phi = \phi_1 = -\phi_2. \tag{4.17}$$

Subject to solution (4.17), (4.14) or (4.15) reduces to

$$-2J_{12} sin\ 2\phi = MsHt_M\ sin\ \phi, \tag{4.18}$$

and by expanding $sin\ 2\phi$, the the magnetization $M = M_s cos\ \phi$ can be expressed as a function of the applied field, H,

$$M = \frac{M_s^2 t_M}{4J_{12}} H, \tag{4.19}$$

i.e., M is linearly proportional to the field, H. Therefore, by measuring the saturation field H_s, we can get the AF coupling strength

$$J_{12} = \frac{1}{4} H_s M_s t_M. \tag{4.20}$$

Complementary measurements using SQUID show that the saturation moment M_s of the 15 Å $Ni_{80}Co_{20}$ layer is about 620 emu/cm^3[25]. From (4.20), the absolute value of AF coupling is about 3.5×10^{-2} erg/cm^2 for the first oscillatory peak at t_{Cu}=8 Å, 5.8×10^{-3} erg/cm^2 for the second peak at t_{Cu}=20 Å, and 6.4×10^{-4} erg/cm^2 for the third peak at t_{Cu}=35 Å.

4.3 Effect of Cumulative Interface Roughness on Magnetization of AF-Coupled $Ni_{80}Co_{20}$/Cu Multilayers

4.3.1 Introduction

A currently debated topic is the influence of interface roughness on the properties of AF-coupled multilayers. Theoretical analyses based on the RKKY model predict that the AF coupling is weakened by the introduction of interface roughness [56], whereas experiments explicitly show that interface roughness introduced by changing the sputtering parameters (e. g., sputtering gas pressure) can enhance the GMR effect[57]. The author of the thesis, in coorperation with other researchers, has specifically studied the effects of cumulative interface roughnes on the magnetic properties of AF-coupled $Ni_{80}Co_{20}$/Cu multilayers[58]. X-ray diffraction was performed for structural characterization and estimating the cumulative interface roughness as a function of bilayer number N. The room temperature in-plane magnetization of the samples was measured using a SQUID magnetometer. The magnetization of the top few layers was studied using SMOKE.

Magnetization measurements from a SQUID magnetometer, which measures the effects of the overall interface roughness, are compared to the SMOKE measurements which are sensitive only to the top few layers where the cumulative interface roughness reaches its maximum value. SMOKE measurements for multilayers with different bilayer number, therefore, give direct information on the effect of cumulative interface roughness on the magnetization process in AF-coupled multilayers.

4.3.2 Samples Preparation and Structural Characterization

Previous studies have shown that ($Ni_{80}Co_{20}$/Cu) multilayers exibit an oscillatory GMR as a function of Cu spacer thickness[25] and a well-defined simple AF coupling for Cu spacer thickness at 20 Å [59]. In order to study the effects of cumulative interface roughness on the magnetization of AF-coupled multilayers, we prepared a series of $Ni_{80}Co_{20}$/Cu multilayers with Cu spacer layer's thickness fixed at 20 Å and bilayer numbers varying from 8 to 100.

($Ni_{80}Co_{20}$15Å/Cu20Å)$\times N$ multilayers with 50 Å thick $Ni_{80}Co_{20}$ buffer layers were deposited on Si substrates. The base pressure before deposition was 2×10^{-7} torr. With a sputtering pressure of 8.5 mtorr of Ar, the deposition rates determined from the measured thickness of single films by low-angle x-ray reflectivity measurements were 1.5 Å/s for $Ni_{80}Co_{20}$ and 1.6 Å/s for Cu.

There are several types of interface imperfections. Cumulative interface roughness is the accumulation of small intrinsic interface roughness in each layer and, therefore, its effects become more pronounced when the number of bilayers increases[60]. Fig. 4.7, extracted from Ref.[60], shows a computer–simulated evolution of cumulative interface roughness with increasing bilayer number N.

Fig. 4.8 shows low-angle x-ray diffraction results for typical samples with different bilayer numbers. All samples exhibit clear first order superlattice Bragg peaks, although the electronic contrast between the two constituent layers is very small. With increasing bilayer number N, the second order superlattice Bragg peaks are gradually damped as shown in Fig. 4.8, suggesting an increase of interface roughness[61]. Clear thickness oscillation fringes between superlattice Bragg peaks are observed for samples with $N < 15$. For a finite film thickness less than 1000 Å, suppression of the fringes with increasing N is partially correlated to the increased outer surface roughness[62]. The low-angle x-ray reflectivity has been analysed using an optical model[62] to produce the outer surface roughness δ_s. Fig. 4.9 shows the decreased intensities of second order superlattice Bragg peaks and increased outer surface roughness with increasing bilayer numbers N.

$Ni_{80}Co_{20}$ and Cu both crystallize in fcc structures with a lattice mismatch of only 2.2%. High-angle $\theta - 2\theta$ x-ray diffraction of ($Ni_{80}Co_{20}$/Cu)$\times$ N multilayers (see Fig. 4.10) shows that the films have textured structures with the dominating fcc (111) direction normal to the film plane and a weak (200) peak. The FWHM of the fcc

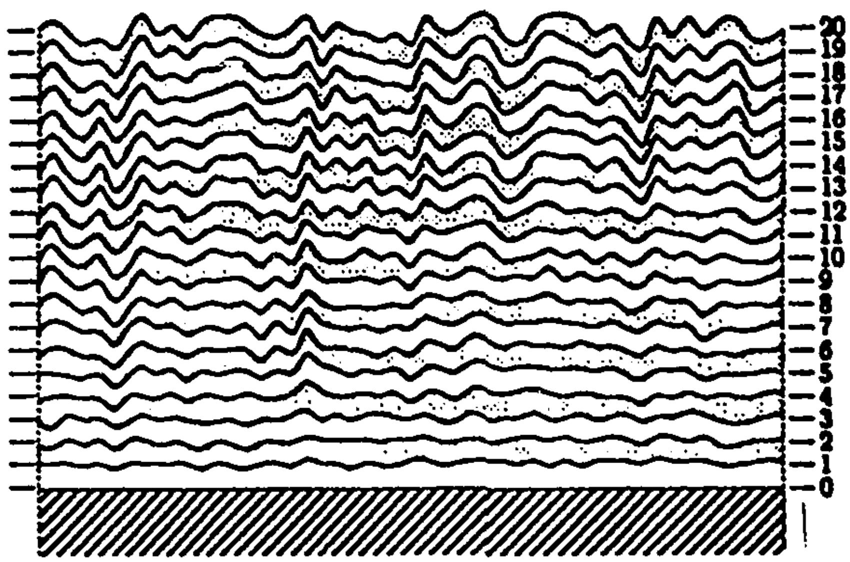

Figure 4.7: Computer-simulated evolution of cumulative interface roughness in an idealised model for multilayer growth.

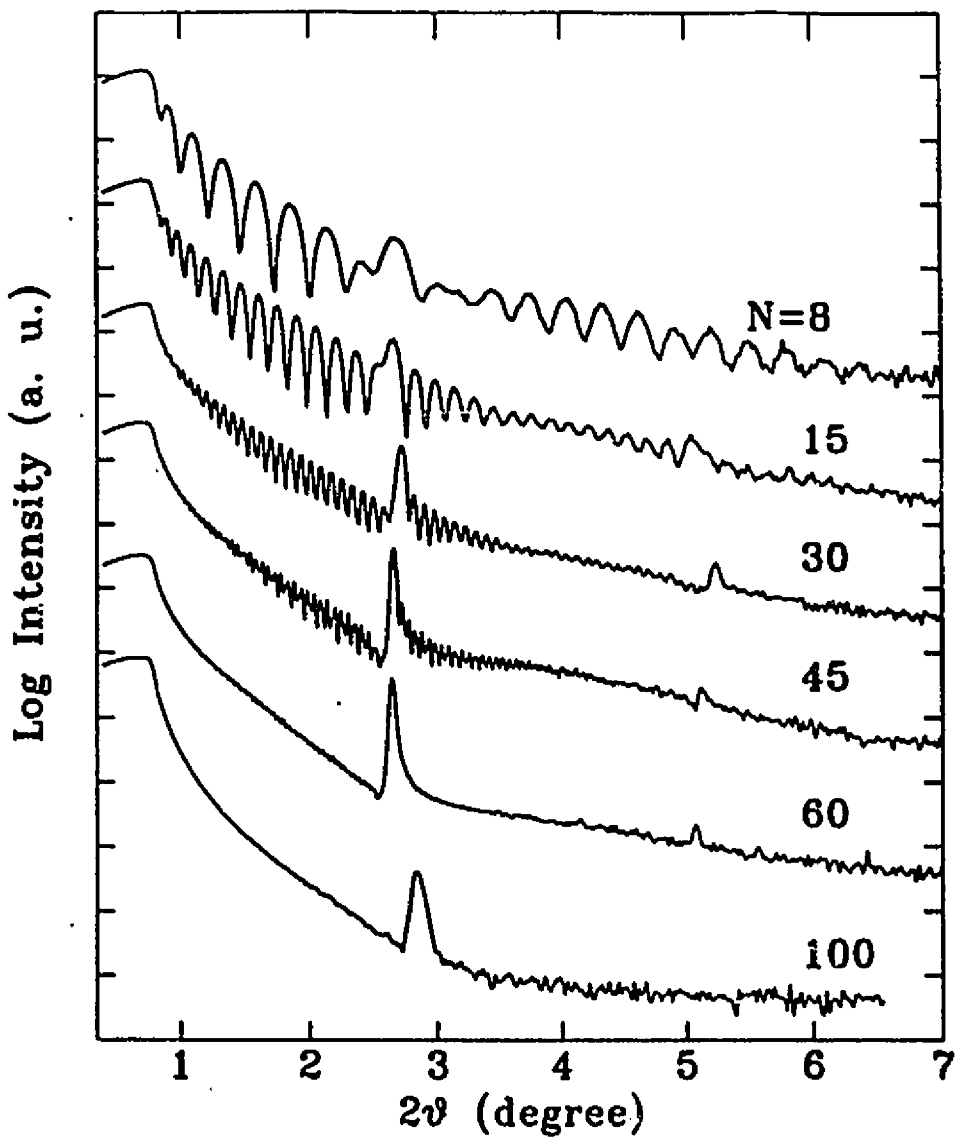

Figure 4.8: Low-angle θ - 2 θ x-ray diffraction spectra of a series of $(Ni_{80}Co_{20}15Å/Cu20Å)\times N$ multilayers. For clarity, the curves have been displaced vertically.

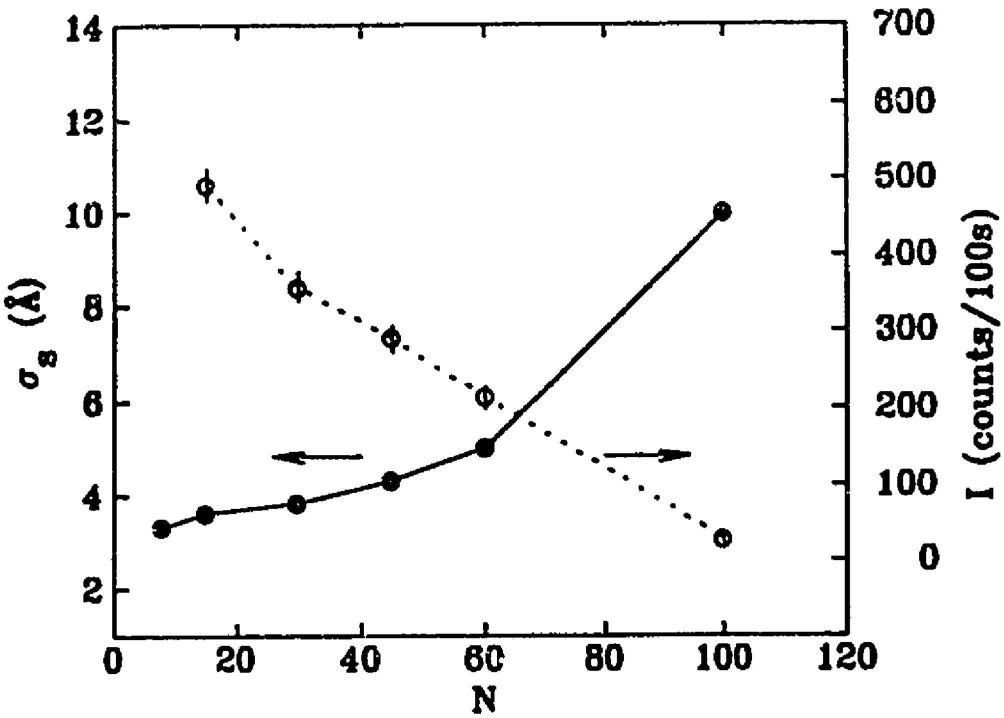

Figure 4.9: Dependence of σ_s and I on N. Where σ_s is the outer surface roughness, and I the intensity of second order superlattice Bragg peaks.

(111) peaks indicate a grain size of about 100 Å.

4.3.3 Effect of Cumulative Interface Roughness on Magnetization

Fig. 4.11(a) shows the overall in-plane magnetization measured with a SQUID magnetometer for a ($Ni_{80}Co_{20}$15Å/Cu20Å)× 45 multilayer having moderate cumulative inteface roughness. The linear magnetization versus field predicted by (4.19) is not observed and there is a distinct nonlinearity for fields $H < H_f$. Fig. 4.11(b) shows the magnetic properties of the top few layers measured by SMOKE. The SMOKE measurements were made using 6328 Å He-Ne laser which has a penetration depth

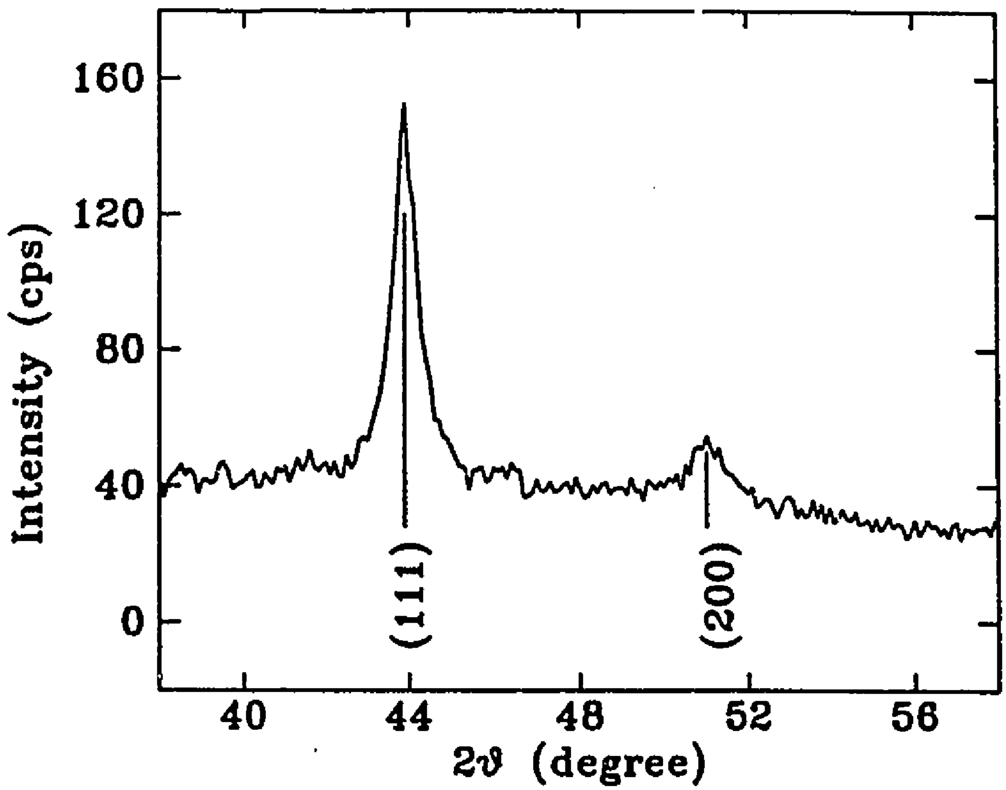

Figure 4.10: High-angle $\theta - 2\theta$ x-ray diffraction spectrum for sample ($Ni_{80}Co_{20}$15Å/Cu20Å)×30.

of about 200 Å corresponding to the top 5 or 6 bilayers of the multilayer. The non-linearity of the magnetization curve for $H < H_f$ is more pronounced for the top few layers than it is for the whole multilayer and the coercivity is considerably increased.

For samples with $N = 8$ both SQUID and SMOKE measurements show a linear M vs H relation below saturation, as shown in Fig. 4.12 and Fig. 4.13, respectively. The saturation moment M_s of the 15 Å $Ni_{80}Co_{20}$ layer is about 620 emu/cm^3, as shown in Fig. 4.12. From 4.20, we can get an AF coupling strength $J \sim 5.8 \times 10^{-3}$ erg/cm^2 for the sample[25]. This value is much smaller than that found in other Cu-based multilayer systems[22,23,63] , indicating a very weak AF coupling between adjacent $Ni_{80}Co_{20}$ layers across 20 Å thick Cu spacer layers. The M_s values measured with the SQUID magnetometer do not depend on N. This implies that the intermixing at the interfaces is not changing significantly with increased interface roughness.

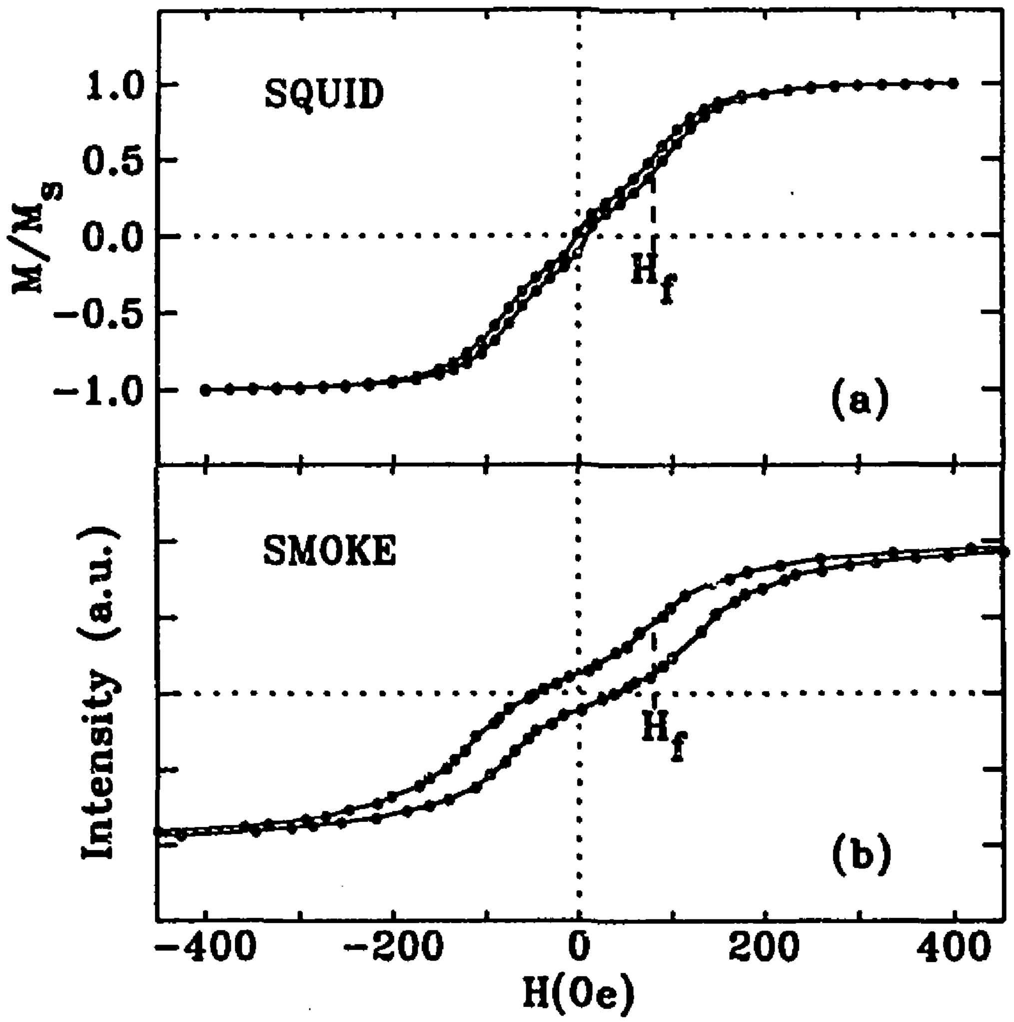

Figure 4.11: Magnetisation of a typical ($Ni_{80}Co_{20}$ 15Å/Cu20Å)×45 sample measured by (a) SQUID (normalised to M_s), and (b) SMOKE (arbitrary unit). It is indicated that for fields $H < H_f$ the nonlinearity of the magnetisation curve can be observed.

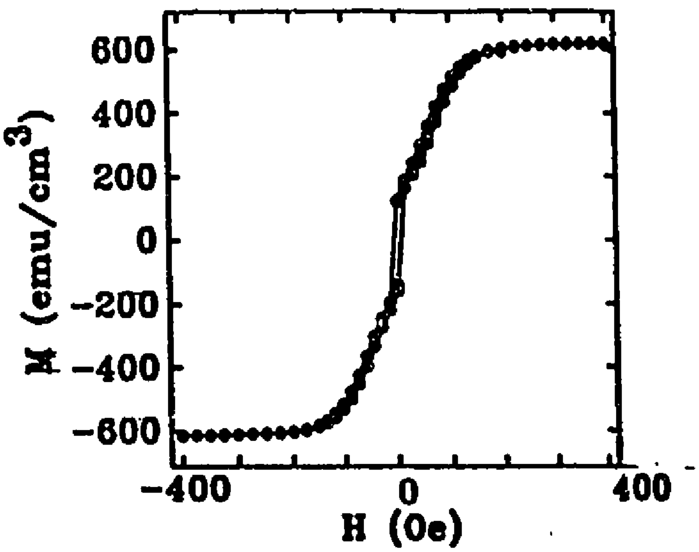

Figure 4.12: SQUID magnetization measurement of sample ($Ni_{80}Co_{20}$ 15Å/Cu20Å)×8. Note that the nearly rectangular loop near zero field is contributed from the 50 Åthick $Ni_{80}Co_{20}$ ferromagnetic buffer.

Fig. 4.13 shows SMOKE measurements for different bilayer numbers. Fig. 4.13(a) shows that the magnetization relation is nearly linear below saturation fields for sample with $N = 8$ where the cumulative interface roughness is presumably small. Fig. 4.13(b) shows results for N=15 where a plateau region with a relatively small slope is observed at low fields, and the failure of the linear $M - H$ relation is clearly seen. As the bilayer number N increases up to 100, the cumulative interface roughness is considerably larger, and the plateau region becomes more striking as indicated in Fig. 4.13(c). From low-angle x-ray reflectivity analyses and SMOKE measurements, we conclude that the nonlinear $M - H$ behavior in samples with large N are related to cumulative interface roughness which becomes significant as the bilayer stacking increases.

The nonlinearity in magnetization is obviously associated with the appearance of significant cumulative interface roughness and might be attributed to an anisotropy related to surface and interface strains due to the roughness.

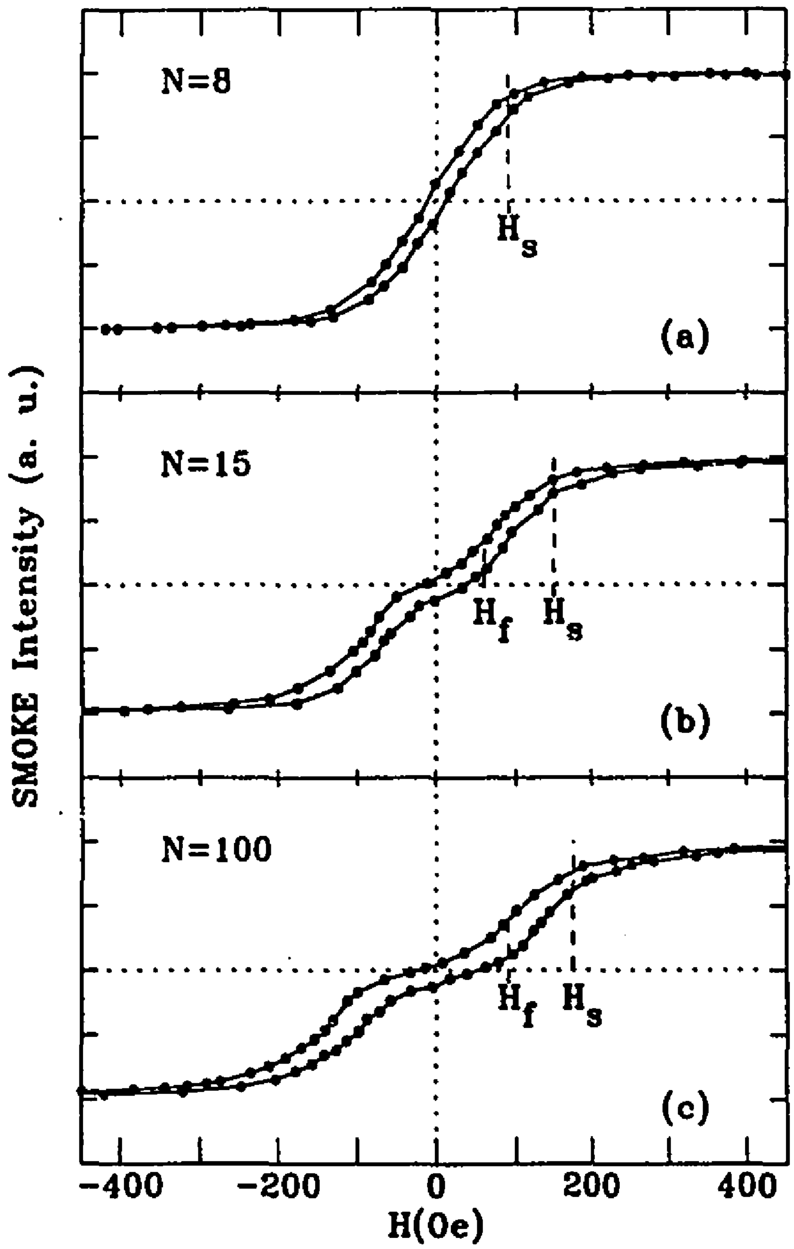

Figure 4.13: SMOKE magnetisation measurements of samples with different bilayer numbers: (a) N=8, (b) N=15 and (c) N=100. Saturation fields H_s and the fields H_f below which the nonlinearity appears are indicated in the figures.

4.3.4 Summary

We have examined the cumulative interface roughness in AF-coupled multilayers ($Ni_{80}Co_{20}$15Å/Cu20Å)$\times N$ using low-angle x-ray reflectivity and SMOKE. Both experiments show that interface roughness increases with the number of bilayer. SMOKE measurements are sensitive to the roughest region of the sample, namely the top several layers. Relatively flat interfaces only exist in sputtered multilayers with bilayer number $N < 10$ for which SMOKE magnetization curves are linear below saturation fields. As the number of bilayers increase, the deviation from linearity in $M - H$ curves gradually becomes larger, which might be attributed to a roughness-related anisotropy.

4.4 Effects of Annealing on Strucutre and Magnetization of AF-Coupled $Ni_{70}Co_{30}/Cu$ Multilayer

Cu-based magnetic multilayers are promising candidates for applications such as MR read heads and magnetic sensors. However, a practical requirement along with a large MR is a high magnetic-field sensitivity, i. e., an appreciable resistance change upon application of a small magnetic field, together with a low coercivity. Identifying multilayer systems with these characteristics remains a key problem in this field.

In the Ni_xCo_{100-x} alloy system, the magnetocrystalline anisotropy is minimum at x=80, while the magnetostriciton coefficient vanishes at x=60[64]. Studies of multilayers with Ni_xCo_{100-x} alloys as magnetic layers and Cu as spacer layers[65] demonstrated that a broad maximum MR of 12% was found in the range x=70–80, and a broad minimum of saturation fields was found in the range x=50–70. It is expected that the choice of x=70 for this multilayer system would combine the advantages of a relatively low magnetocrystalline anisotropy and a small magnetostriciton coefficient, and result in a substantial GMR with a low saturation field, and hence a large field sensitivity. In this section, we will focus on the AF-coupled $Ni_{70}Co_{30}/Cu$ multilayer.

In order to reduce the influence of cumulative interface roughness on the magnetization of multilayers, we design a sample with 10 bilayers. We sputtered a series of ($Ni_{70}Co_{30}$15Å/Cu t_{Cu}Å)×10 samples with 15 Å $Ni_{70}Co_{30}$ buffer layers on Si wafers. The thickness of Cu spacer layer t_{Cu} varied from 17 Å to 21 Å with 1 Å step. The base pressure before sputtering was 2×10^{-7} Torr. The Ar pressure during sputtering is 8.5 mT. All samples' magnetization loops were measured using SMOKE, and the sample with the maximum AF coupling strength was identified by the maximum saturation field. It was found that the sample with t_{Cu}=20 Å shown the the maximum saturation field 120 Oe.

The SMOKE loop of sample ($Ni_{70}Co_{30}$15Å/Cu20Å)×10 is shown in Fig. 4.14. The

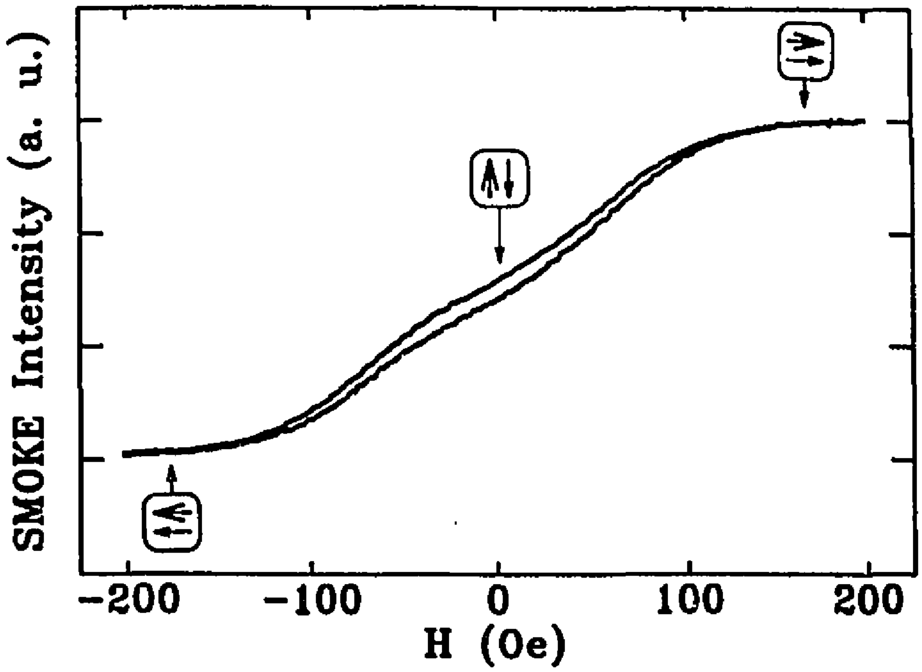

Figure 4.14: SMOKE loop of ($Ni_{70}Co_{30}$15Å/Cu20Å)×10 multilayer. Magnetisation configurations are illustrated in the figure by arrows which depict submagnetisation vectors.

magnetization is nearly linear before saturation with very small hysteresis, which is quite close to the relation (4.19) based on a 'single-domain limit'.

Because multilayer systems are not in the thermodynamic equilibrium, their structure is sensitive to growth conditions including, for example, the deposition method, the sputtering gas pressure, the substrate material and the buffer layer. Experiments reveal that the structure and physical properties of multilayers containing Cu layers are particularly sensitive to deposition conditions, both for sputtered and MBE prepared multilayers[19]. After-growth annealing also has effects on the structure of multilayers, and in turn influences the magnetic properties of multilayers.

We annealed the AF-coupled ($Ni_{70}Co_{30}$15Å/Cu20Å)×10 sample up to 400^{0}C. The sample was placed, together with a temperature probe, inside a quartz glass tube which was exacuvated to a pressure of 10^{-3} Torr. The sample was annealed in a gas of mixture consisting of 5% H_2 and 95% Ar in a temperature-controlled furnace at different temperature steps for ten minutes, respectively, and then cooled to room temperature.

In order to reveal the influence of annealing on the the sample's crystalline structure, conventional high-angle x-ray diffraction was measured. Fig. 4.15 shows the spectra on the sample annealed continually at different temperatures. All spectra show textured structures with the fcc (111) direction normal to the film plane. The FWHM of the fcc (111) peaks decreases monotically with each annealing step although the peak positions remain unchanged, indicating that the film has developed larger textured grains with no evidence for formation of phase segregated regions. When annealing up to temperatures larger than 250^0, weak (200) peaks gradually appear.

Changes in the magnetic behaviour of the film was also monitored after each step using SMOKE. Fig. 4.16 shows SMOKE hysteresis loops for the film annealed at different temperatures. Compared with the as-deposited stage, the film annealed at moderate temperatures up to 200^0C possesses an unchanged saturation field with smaller hyseresis, which is noted to be consistent with an enlarged grain size. Annealing up to 300^0C gives rise to almost square loops, typical of a ferromagnetic film. This suggests that the interdiffusion at interfaces between $Ni_{70}Co_{30}$ and Cu layers becomes severe, and Cu spacer layers' thickness is narrowed and much smaller than 20 Å, the thickness required for the AF coupling interaction to be maintained. Further annealing up to 400^0 destroys the multilayer structure of the film, and an alloy forms between Cu and $Ni_{70}Co_{30}$. This NiCoCu system shows ferromagnetic hysteresis with a much larger coercivity, as seen in Fig. 4.16(e).

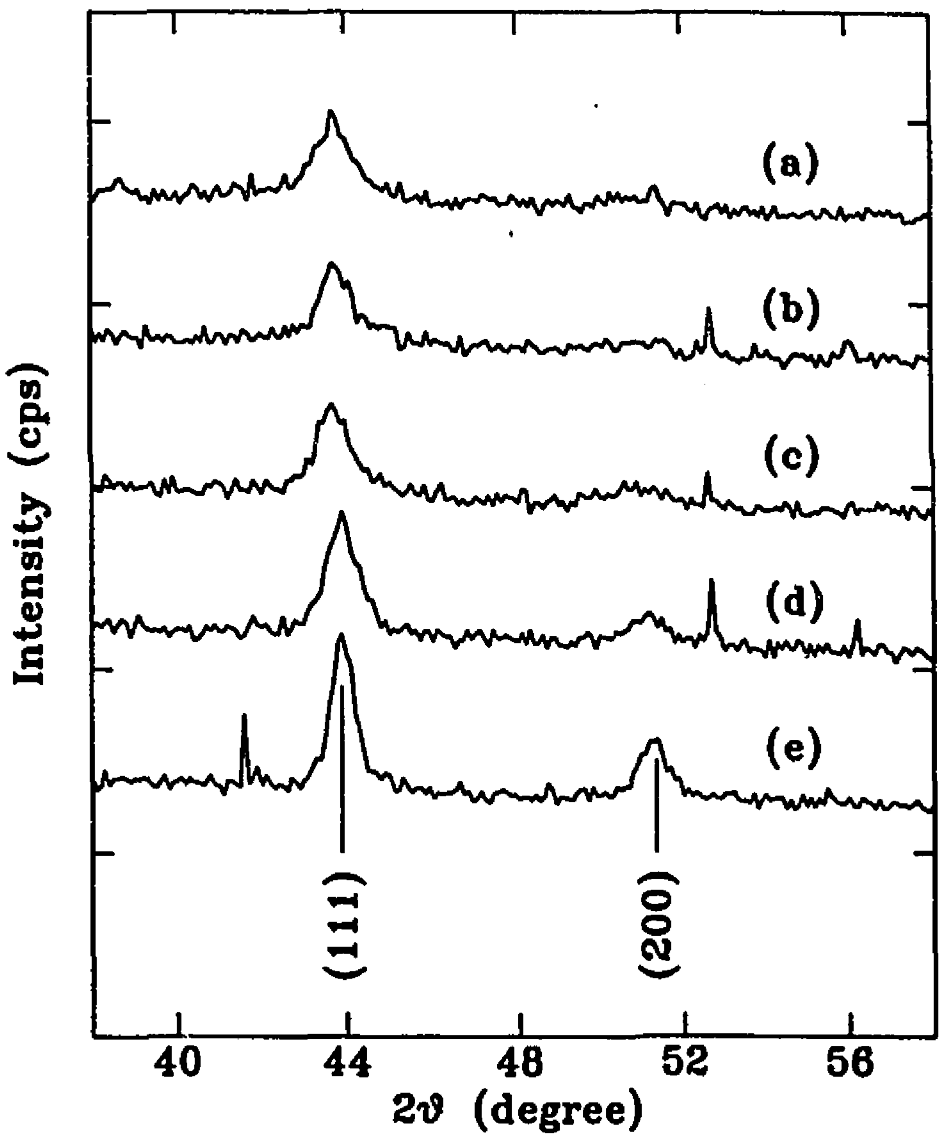

Figure 4.15: High-angle diffraction spectra for multilayer sample ($Ni_{70}Co_{30}$15Å/Cu20Å)×10 annealed continually at different temperatures: (a) as-deposited; (b) 200°C; (c) 250°C; (d) 300°C; and (e) 400°C. For clarity, the curves have been displaced vertically.

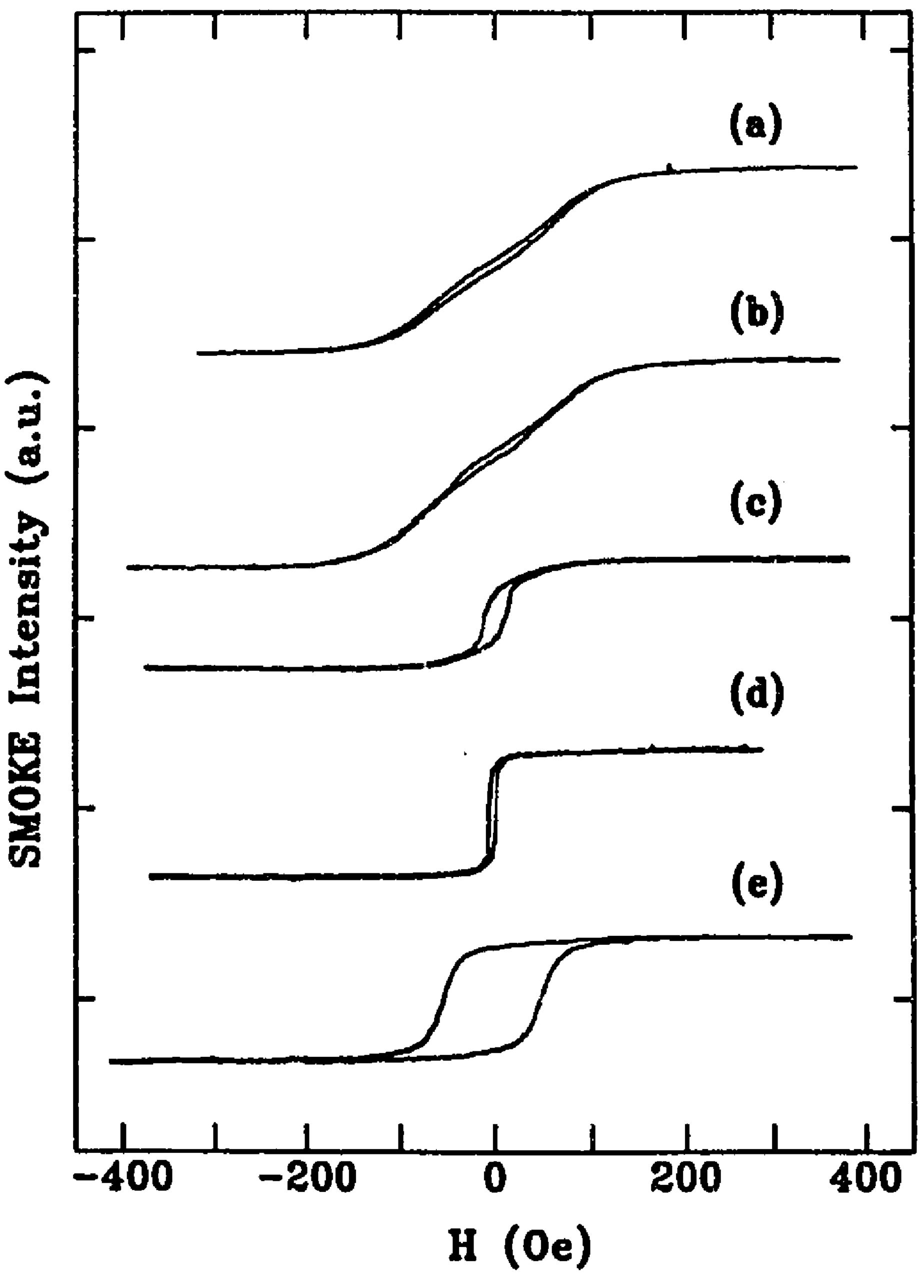

Figure 4.16: SMOKE hysteresis loops for multilayer sample ($Ni_{70}Co_{30}$15Å/Cu20Å)×10 annealed continually at different temperaturesi: (a) as-deposited; (b) 200°C; (c) 250°C; (d) 300°C; and (e) 400°C.

4.5 Magnetization Configurations in Multilayer with Unequal Magnetic Layer Thicknesses

Most of previous studies of AF-coupled multilayers have concentrated on samples containing magnetic layers with equal thicknesses. The magnetization behaviour is then well understood. Recently there has been a growing interest in sandwich structures with unequal thicknesses of magnetic layers[66]. Here we will study the magnetization behaviour of a multilayer system with unequal thicknesses, $t_1 < t_2$, of the adjacent magnetic layers.

We sputtered a multilayer ($Ni_{70}Co_{30}$15Å/Cu20Å/$Ni_{70}Co_{30}$30Å/Cu20Å)×5 with a 15 Å $Ni_{70}Co_{30}$ buffer layer on Si wafer. The base pressure before sputtering was 2×10^{-7}Torr. The Ar pressure during sputtering is 8.5 mT.

The SMOKE loop of this sample is shown in Fig. 4.17. Analyses of magnetization process reveals that the thicker and the thinner magnetic layers are AF-coupled at zero field, and the application of a small field aligns the thicker magnetic layer nearly parallel to the field, while the adjacent thinner magnetic layer, is nearly antiparallel to the thicker magnetic layer due to the dominating AF coupling interaction between them. When the saturation field is reached, all magnetic layers are aligned parallel to the field. Magnetization configurations were shown in the figure by arrows which depict magnetization vectors in the adjacent magnetic layers.

From the hysteresis loop, we can observe two anti-parallel magnetization configurations near the zero field along each direction of the applied field. Due to the AF coupling interaction, the magnetizations in the adjacent unequal magnetic layers tends to be in the anti-parallel configuration. Around the zero field, the anti-parallel magnetization, meanwhile perpendicular to the applied field, gives rise to a nearly zero magnetization projection upon the field direction. This anti-parallel magnetization configuration is marked by plateau B. A small field pulls the magnetization of the 30 Å thick magnetic layers lie along the the field direction with that of the 15 Å magnetic layers opposite, and results in a nearly 1/3 net magnetization projection

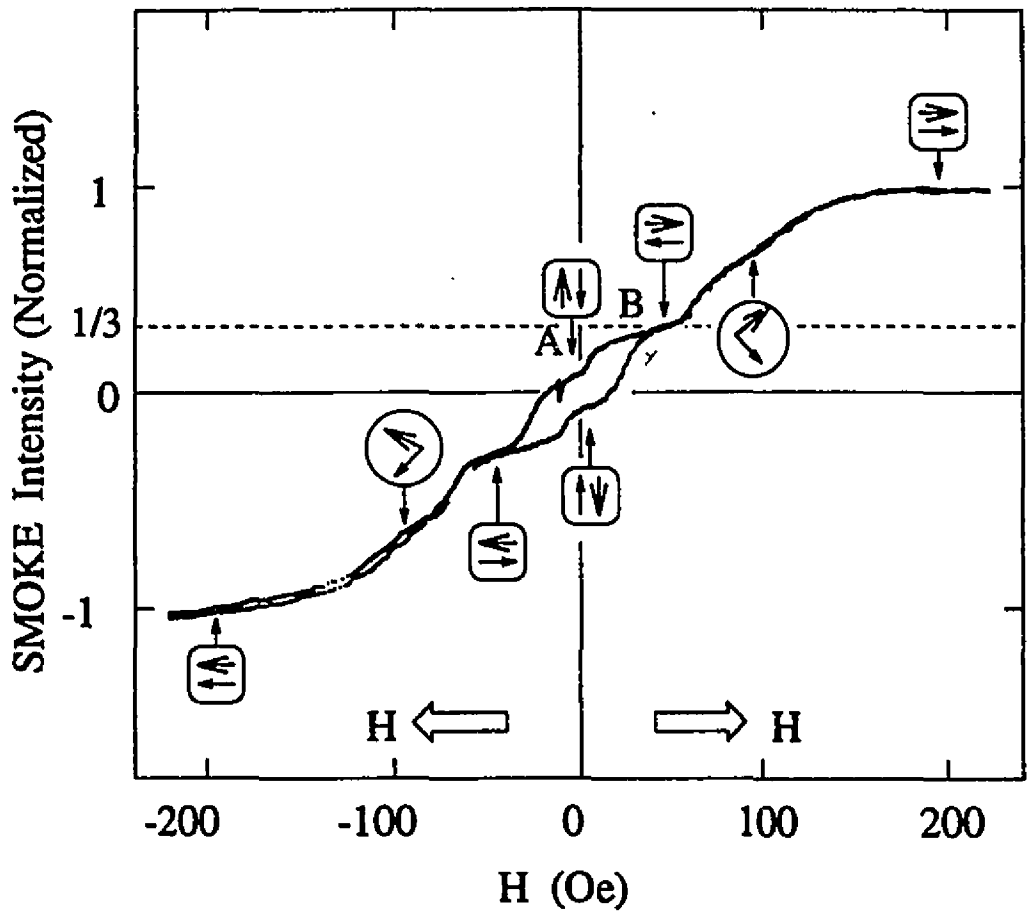

Figure 4.17: SMOKE loop of ($Ni_{70}Co_{30}$15Å/Cu20Å/$Ni_{70}Co_{30}$30Å/Cu20Å)×5 multilayer.

upon the field direction. This anti-parallel magnetization configuration is marked by plateau A. The further application of the field tends to rotate all magnetizations up to the field direction until the saturation parallel configuration is reached.

For comparison, the MR data on the sample are displayed in Fig. 4.18. The field dependence of MR is consistent with that of magnetization, suggesting their common origin in the change in relative orientations of adjacent magnetic layers in response to the applied field.

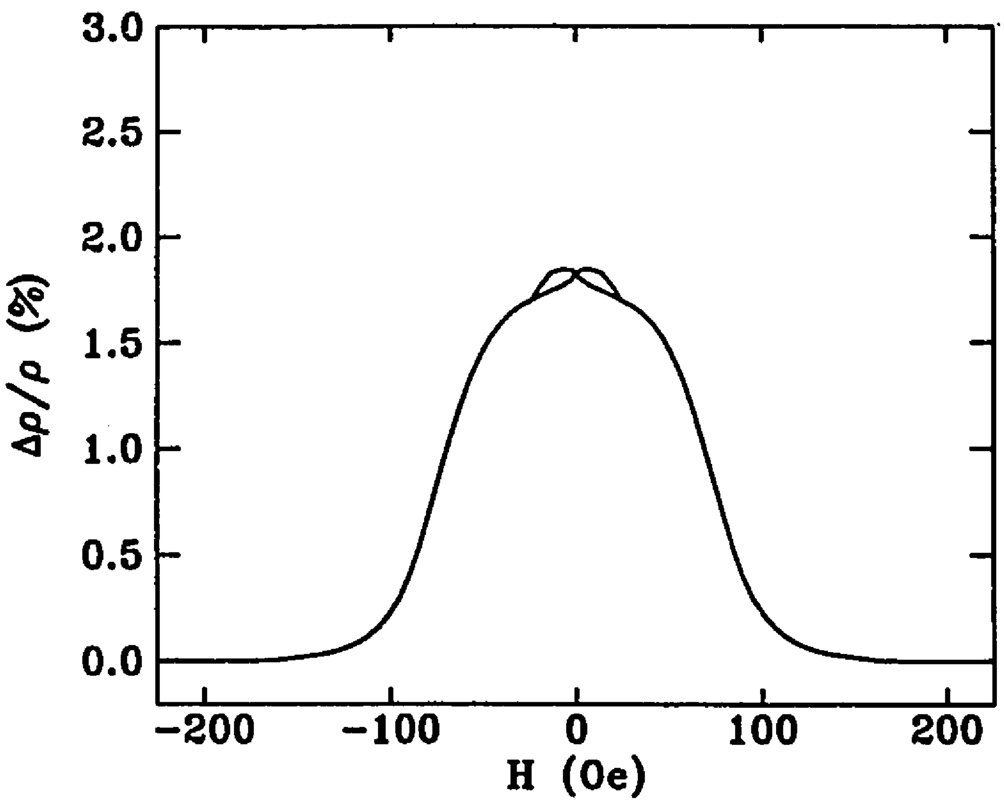

Figure 4.18: Magnetoresistance $[\Delta\rho/\rho = (\rho_0 - \rho(H_s))/\rho(H_s)]$ vs applied magnetic field at room temperature for ($Ni_{70}Co_{30}$10Å/Cu20Å/$Ni_{70}Co_{30}$15Å/Cu20Å)×5 multilayer.

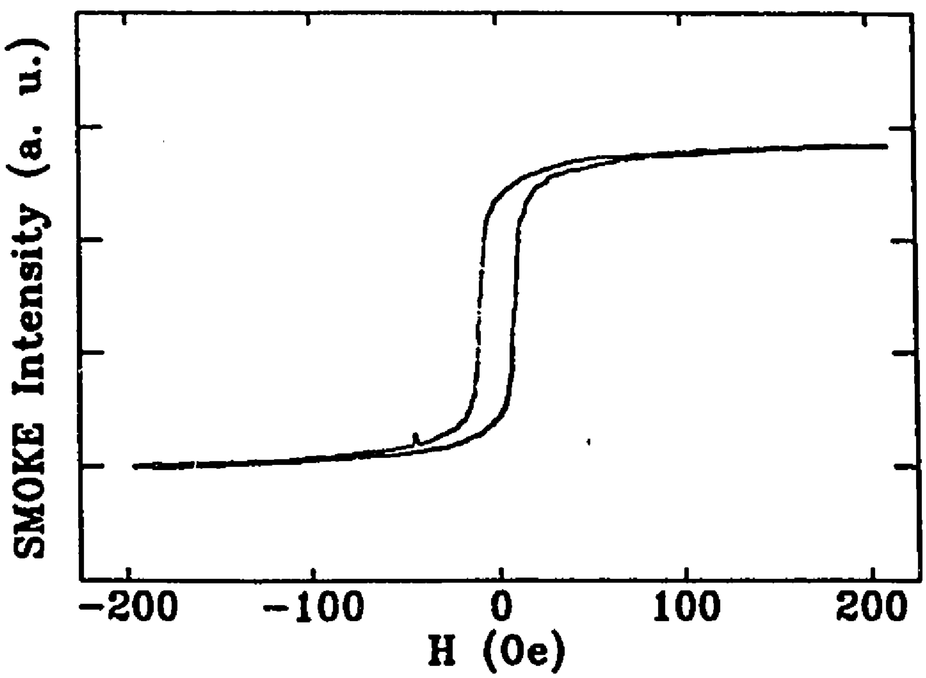

Figure 4.19: SMOKE loop of ($Ni_{70}Co_{30}$15Å/Cu35Å)×10 multilayer.

4.6 Magnetization Configurations of Multilayer Coupled under Two Different AF Coupling Strengthes

We prepared a series of multilayer samples near the next oscillatory coupling peak using the same sputtering condition which we used to sputter ($Ni_{70}Co_{30}$15Å/Cu20Å)×10 multilayer. Through SMOKE measurements, it was found that the next maximum AF coupling occured at t_{Cu}=35 Å. SMOKE loop for this sample is shown in Fig. 4.19. The saturation field is 20 Oe.

In order to study the magnetization behaviour in a multilayer where a magnetic layer is AF-coupled with its two magnetic layer neighbors with two different coupling

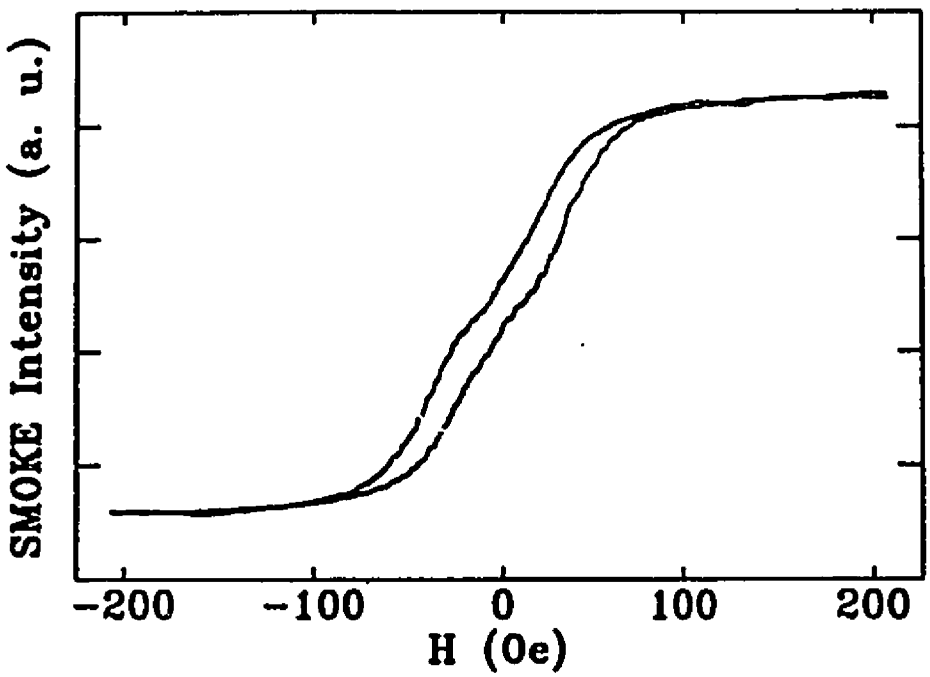

Figure 4.20: SMOKE loop of $(Ni_{70}Co_{30}15Å/Cu20Å/Ni_{70}Co_{30}15Å/Cu35Å)\times5$ multilayer.

strengthes J_1 and J_2, we sputtered $(Ni_{70}Co_{30}15Å/Cu20Å/Ni_{70}Co_{30}15Å/Cu35Å)\times5$ multilayer sample. The SMOKE loop of this sample is shown in Fig. 4.20. A linear $M-H$ relation can be observed with a saturation field of 70 Oe which is the average of the values found in sample $(Ni_{70}Co_{30}15Å/Cu20Å)\times10$ whose saturation field is 120 Oe, and sample $(Ni_{70}Co_{30}15Å/Cu35Å)\times10$ whose saturation field is 20 Oe.

For a multilayer system containing two different AF coupling strengthes J_1 and J_2, the energy per area is

$$E=(J_1+J_2)cos\,(\phi_1-\phi_2)-M_sHt_M(cos\,\phi_1+cos\,\phi_2). \tag{4.21}$$

Just like the AF-coupled multilayer containing only one coupling strength, the stable configuration of magnetizations of adjacent magnetic layers is found by energy minimization, and the $M - H$ relation is found to be

$$M = \frac{M_s^2 t_M}{2(J_1 + J_2)} H \tag{4.22}$$

which gives a saturation field

$$H_s = \frac{2(J_1 + J_2)}{M_s t_M}. \tag{4.23}$$

Thus the value of saturation field is the average of the values found in the two multilayer systems, each of which contains a single AF coupling strength. This theoretical expectation was observed in SMOKE hysteresis measurements on ($Ni_{70}Co_{30}$15Å/Cu20Å/$Ni_{70}Co_{30}$15Å/Cu35Å)×5 multilayer sample.

Chapter 5

Conclusions

An apparatus measuring magneto-optic Kerr effect (MOKE) has been designed and constructed. Phenomenologically, magnetization in a medium changes its dielectric properties and results in the variation of optic modes of electromagnetic radiation in it; hence, the connection between magnetization of the medium and variation in polarization of reflected beam from the medium's mirror surface is established. The magnetization loop is recorded by a computer-controlled data-aquisition system or simply by an X–Y recorder.

This apparatus can be used for magnetic characterization of multilayers. In the thin-film limit, the surface magneto-optic Kerr effect (SMOKE) measured on a magnetic multilayer is a measurement of the average magnetization of several magnetic layers near the film's outer surface. This apparatus has been employed in several other researches[59,67,68].

SMOKE measurements on a series of sputtered $Ni_{80}Co_{20}15Å/Cut_{Cu}$ multilayers confirmed that the coupling strength in these multilayers oscillated from antiferromagnetic (AF) coupling to ferromagnetic coupling as a function of Cu spacer layer thickness t_{Cu}, and three oscillatory peaks at t_{Cu}=8 Å, 20 Å and 35 Å were observed.

Effects of cumulative interface roughness on the magnetization of AF-coupled $(Ni_{80}Co_{20}15Å/Cu20Å)\times N$ were investigated as a function of bilayer number N. Low-angle x-ray reflectivity revealed that cumulative interface roughness increased with increasing N. SMOKE measuremets, which only detected the top $5 \sim 6$ bilayers due to the 200 Å penetration depth, shown that saturation fields and coercivities increased with increasing N, possibly due to an out-of-plane anisotropy associated with cumulative interface roughness in multilayers.

$Ni_{70}Co_{30}$ was chosen as the magnetic layer for its intrinsically low magnetocrystalline anisotropy and small magnetostriction coefficient, and AF-coupled $Ni_{70}Co_{30}$15Å/Cu20Å multilayer was sputtered. SMOKE measurement on this sample shown a nearly linear $M-H$ relation before saturation, which obeyed the theoretical prediction in the single-domain limit. This sample was continually heat-treated up to 400°C in several steps. High-angle x-ray diffraction and SMOKE measurement were made on the sample after each step. Annealing up to 200°C gave rise to larger grain sizes in the film and improved the AF coupling between its magnetic layers across Cu spacer; annealing up to 250°C began to cause significant interdiffusion at the interfaces of $Ni_{70}Co_{30}$ and Cu and weakened the AF coupling; annealing up to 300°C brought about the failure of AF coupling; and annealing up to 400°C rendered the film ferromagnetic with a much larger coercivity, possibly due to the formation of CuNiCo alloy in the film.

($Ni_{70}Co_{30}$15Å/Cu20Å/$Ni_{70}Co_{30}$30Å/Cu20Å)×5 multilayer was prepared for studying the AF coupling between magnetic layers of unequal thicknesses. SMOKE measurement revealed two stable anti-parallel magnetization configurations at small field. MR measurement provided a complimentary evidence of the configurations.

Finally, ($Ni_{70}Co_{30}$15Å/Cu20Å/$Ni_{70}Co_{30}$15Å/Cu35Å)×5 multilayer was prepared for studying the magnetic behaviour in a multilayer where a magnetic layer was AF-coupled with its two magnetic layer neighbors with two different coupling strengthes. A linear $M-H$ relation was observed with a saturation field which was the average of the values in the two multilayer systems each of which contained a single AF coupling strength, much to the expectation based on a theoretical consideration in single-domain limit.

References

[1] M. Faraday, Trans. Roy. Soc. (London)5, 592(1846).

[2] J. Kerr, Phil. Mag. 5, 161(1878).

[3] C. C. Robinson, J. Opt. Soc. Am. **53**, 681(1963).

[4] J. C. Suits, Rev. Sci. Instrum. **42**, 19(1971).

[5] K. Sato, Japan. J. of Appl. Phys. **20**, 2403(1981).

[6] F. Schmidt, W. Rave, and A. Hubert, IEEE Trans. Magnetics, **21**, 1596(1985).

[7] For recent reviews, see for example, I. K. Schuller, J. Guimpel, and Y. Bruynseraede, MRS Bulletin, Vol. XV, No.2, 37(1990).

[8] For recent reviews, see for example, B. M. Clemens, and R. Sinclair, MRS Bulletin, Vol. XV, No.2, 19(1990).

[9] For recent reviews, see for example, A. L. Greer, and F. Spaepen, in *Synthetic Modulated Structures*, edited by L. L. Chang, and B. C. Giessen(Academic Press, New York, 1985).

[10] For recent reviews, see for example, B. N. Engel, and C. M. Falco, MRS Bulletin, Vol. XV, No. 9, 37(1990).

[11] P. Grünberg, R. Schreiber, Y. Pang, M. N. Brodsky, and H. Sowers, Phys. Rev. Lett. **57**, 2442(1986).

[12] S. S. P. Parkin, N. More, and K. P. Roche, Phys. Rev. Lett. **64**, 2304(1990).

[13] M. N. Baibich, J. M. Broto, A. Fert, F. Nguyen van Dau, F. Petroff, P. Etienne, G. Creuzet, A. Friederich, and J. Chazelas, Phys. Rev. Lett. **61**, 2472(1988).

[14] For recent reviews, see for example, *Thin Film Growth Techniques for Low-Dimensional Structures*, edited by R. F. C. Farrow *et al.*(Plenum Press, New York,1987).

[15] For recent reviews, see for example, *Growth, Characterization and Properties of Ultrathin Magnetic Films and Multilayers*, edited by B. T. Jonker, J. P. Heremans and E. E. Marinero (Mater. Res. Soc. Symp. Proc. **151**, Pittsburgh, 1989).

[16] T. Shinjo, and T. Takada, in *Ferromagnetic Materials (3)* (Elsevier, Amsterdam, 1987).

[17] P. Grüberg, and F. Saurenbach, MRS Int'l. Mtg. Adv. Mats. **10**, 255(1989).

[18] For the review, see for example, R. M. White, *Quantum Theory of Magnetism* (Springer-Verlag, Berlin, 1983).

[19] S. S. P. Parkin, R. Bhadra, and K. P. Roche, Phys. Rev. Lett. **66**, 2152(1991).

[20] S. S. P. Parkin, Phys. Rev.Lett. **67**, 3598(1991).

[21] G. Binasch, P. Grüberg, F. Saurenbach, and W. Zinn, Phys. Rev. B**39**, 4828(1989).

[22] S. S. P. Parkin, Appl. Phys. Lett. **60**, 512(1992).

[23] M. Jimbo, T. Kanda, S. Goto, and S. Tsunashima, Jpn. J. Appl. Phys. **31**, L1348(1992).

[24] X. Bian, J. O. Ström-Olsen, Z. Altounian, Y. Huai, and R. W. Cochrane, J. Appl. Phys. **75**, 6560(1994).

[25] X. Bian, J. O. Ström-Olsen, Z. Altounian, Y. Huai, and R. W. Cochrane, Appl. Phys. Lett. **62**, 3525(1993).

[26] P. N. Argyres, Phys. Rev. **97**, 334(1955).

[27] L. D. Landau, and E. M. Lifshitz, *Electrodynamics of Continuous Media* (Addison-Wesley, Reading, 1960), Chapter 11.

[28] M. Born, and E. Wolf, *Principles of Optics* (MacMillan, New York, 1964), page 28.

[29] Ref. [28], page 27.

[30] L. D. Landau, and E. M. Lifshitz, *Statistical Physics* (Addison-Wesley, Reading, 1958), section 119.

[31] Ref. [27], page 314.

[32] W. Voigt, *Magneto-und Electrooptic* (Teuner, Leipzig, 1908); *Handbuch der Electrizität und des Magnetismus* Vol. IV:2(Barth, Leipzig, 1915), page 393.

[33] Ref. [28], page 613.

[34] C. C. Robinson, J. Opt. Soc. Am. **51**, 1316(1962); **53**, 681(1963).

[35] For example, K. L. Chopra, *Thin Film Phenomena* (McGraw-Hill, New York, 1969).

[36] X. Bian, private communication.

[37] For recent review, see, for example, D. B. McWhan, in *Physics, Fabrication and Applications of Multilayered Structures* (Plenum, New York, 1988), edited by P. Dhez and C. Weisbuch, pg 67.

[38] E. E. Fullerton, I. K. Shuller, H. Vanderstraeten, and Y. Bruynseraede, Phys. Rev. B**45**, 9292(1992).

[39] M. F. Toney, and S. Brennan, J. Appl. Phys. **66**, 1861(1989).

[40] E. E. Fullerton, I. K. Schuller, and Y. Bruyseraede, MRS Bulletin/December, 33 (1992).

[41] Y. Shi, Ph. D Thesis , McGill University, 1992.

[42] Y. Huai, and R. W. Cochrane, J. Appl. Phys. **72**, 2523(1992).

[43] X. Bian, and Y. Huai, private communication.

[44] P. H. Lissberger, J. Opt. Soc. Am. **51**, 948(1990).

[45] J. M. Ballantyne, J. Opt. Soc. Am. **54**, 1352(1964).

[46] S. Takana, Japan. J. Appl. Phys. **2**, 548(1963).

[47] G. Metzger, P. Pluvinage, and R. Torguet, Ann. Phys. (Paris) **10**, 5(1965).

[48] T. Yoshino, and S. Tanaka, Japan. J. Appl. Phys. **5**, 989(1966).

[49] S. D. Bader, E. R. Moog, and P. Grünberg, J. Magn. Magn. Mat. **53**, L295(1986).

[50] S. D. Bader, E. R. Moog, J. Appl. Phys. **61**, 3729(1986).

[51] C. Liu, E. R. Moog, and S. D. Bader, Phys. Rev. Lett. **60**, 2422(1988).

[52] E. R. Moog, C. Liu, S. D. Bader, and J. Zak, Phys. Rev. **B39**, 6949(1988).

[53] J. Zak, E. R. Moog, C. Liu, and S. D. Bader, J. Appl. Phys. **68**, 4203(1990).

[54] Z. Q. Qiu, J. Pearson, and S. D. Bader, Phys. Rev. **B45**, 7211(1992).

[55] R. E. Camley and J. Barnaś, Phys. Rev. Lett. **63**, 664(1989); J. Barnaś, A. Fuss, R. E. Camley, P. Grünberg, and W. Zin, Phys. Rev. **B42**, 8110(1990).

[56] R. Coehoorn, Phys. Rev. **B44**, 9331(1991).

[57] E. E. Fullerton, D. M. Kelly, J. Guimpel, and I. K. Shuller, Phys. Rev. Lett. **68**, 859(1992).

[58] X. Meng, X. Bian, R. Abdouche, W. B. Muir, J. O. Strö-Olsen, Z. Altounian, and M. Sutton, J. Appl. Phys. **76**, (1994), in press.

[59] X. Bian, J. O. Ström-Olsen, Z. Altounian, B. D. Gaulin, C. V. Stager, and J. A. Avelar, Phys. Rev. **B50**, 3114(1994).

[60] A. P. Payne, and B. M. Clemens, Phys. Rev. **B47**, 2289(1003).

[61] F. J. Lamelas, H. David He, and Roy Clark, Phys. Rev. **B43**, 12296(1991).

[62] Y. Huai, R. W. Cochrane, and M. Sutton, Phys. Rev. **B48**, 2568(1993).

[63] D. H. Mosca, F. Petroff, A. Fert, P. A. Schroeder, W. P. Pratt Jr., and R. Laloee, J. Magn. Magn. Mat. **94**, L1(1991).

[64] T. R. McGuire and R. L. Potter, IEEE Trans. Magn. **MAG-11**, 1018(1975).

[65] X. Bian, J. O. Strö-Olsen, Z. Altounian, Y. Huai, and R. W. Cochrane, J. Appl. Phys. **75**, 7064(1994).

[66] W. Folkerts, and S. T. Purcell, J. Magn. Magn. Mater. **111**, 306(1992).

[67] H. Zhang, R. W. Cochrane, Y. Hui, M. Mao, X. Bian, and W. B. Muir, J. Appl. Phys. **75**, 6534(1994).

[68] X. Bian, X. Meng, J. O. Strö-Olsen, Z. Altounian, W. B. Muir, M. Sutton, and R. W. Cochrane, J. Appl. Phys. **76**, (1994), in press.